Focused-helium-ion-beam blow forming of nanostructures: radiation damage and nanofabrication

Chung-Soo Kim[1,5], Richard G Hobbs[2,5] , Akshay Agarwal[1] , Yang Yang[3], Vitor R Manfrinato[1], Michael P Short[3], Ju Li[3,4] and Karl K Berggren[1,5]

[1] Research Laboratory of Electronics, Massachusetts Institute of Technology, Cambridge, MA, 02139, United States of America
[2] School of Chemistry, Advanced Materials and Bioengineering Research (AMBER) Centre and Centre for Research in Adaptive Nanostructures and Nanodevices (CRANN), Trinity College Dublin, Dublin, Ireland
[3] Department of Nuclear Science and Engineering, Massachusetts Institute of Technology, Cambridge, MA, 02139, United States of America
[4] Department of Materials Science and Engineering, Massachusetts Institute of Technology, Cambridge, MA, 02139, United States of America

E-mail: reaves.kim@gmail.com, hobbsr@tcd.ie and berggren@mit.edu

CrossMark

Abstract

Targeted irradiation of nanostructures by a finely focused ion beam provides routes to improved control of material modification and understanding of the physics of interactions between ion beams and nanomaterials. Here, we studied radiation damage in crystalline diamond and silicon nanostructures using a focused helium ion beam, with the former exhibiting extremely long-range ion propagation and large plastic deformation in a process visibly analogous to blow forming. We report the dependence of damage morphology on material, geometry, and irradiation conditions (ion dose, ion energy, ion species, and location). We anticipate that our method and findings will not only improve the understanding of radiation damage in isolated nanostructures, but will also support the design of new engineering materials and devices for current and future applications in nanotechnology.

Supplementary material for this article is available online

Keywords: focused helium ion beam, diamond, nanofabrication, plastic deformation, ion range, helium nanocavitation

(Some figures may appear in colour only in the online journal)

Introduction

Ion irradiation has been used extensively to tune the mechanical [1–3], optical [4–6], electrical [4, 6, 7], and chemical [8, 9] properties of materials, as well as for nanofabrication [6, 8, 10–12]. Understanding the response of materials to ion irradiation is especially important for the design of engineering materials, such as radiation-tolerant materials for nuclear reactors [3, 13–15], for ion implantation in semiconductors and for nanofabrication. In nanostructures, finely focused ion beams may play a critical role in locally modifying materials. For example, focused gallium ion beams (FGIB) have been used extensively for local modification of materials such as surface hardening [2], wire straightening [16], and nanowire growth [17]. Helium ion microscopy (HIM), facilitated by the development of gas field ion sources and sub-nanometer-diameter focused helium ion beams (FHIB), has opened up new avenues for imaging [18] and single-nanometer scale fabrication [19]. Potential impacts of HIM on nanoscience include nanometrology for critical

[5] Authors to whom any correspondence should be addressed.

1

dimension measurement [20], biological imaging [21], and nanofabrication for plasmonic antennas [22], nanopores [23], transmission electron microscopy (TEM) lamellae [24], photomask repair [25], and circuit editing [26]. Local modification of materials and defect creation via FHIB at the nanoscale has also been applied to quantum optics [27] and circuits [28, 29].

Understanding He^+ scattering in materials is critical to the use of FHIB to control material properties. In general, the distribution of FHIB-induced damage in materials depends on (1) the scattering ranges of helium in the material, (2) the sputtering yield and (3) helium solubility in the material. (1) Radial scattering and ion ranges of He^+ in materials are approximately twelve times larger than that of Ga^+ with equivalent kinetic energy since the stopping power of He^+ is about twelve times lower than that of Ga^+. (2) The sputtering yield of He^+ is two orders of magnitude lower than that of Ga^+ for the materials studied in this work (carbon and silicon). This difference arises because He^+ loses energy primarily via electronic interactions with fewer atomic displacements than observed for Ga^+. Also, Ga^+-induced damage can reach a steady-state condition, resulting in a constant Ga^+ implantation profile by continuous surface recession due to sputtering [30]. (3) Helium has primarily repulsive interactions with host material atoms due to its closed-shell electron configuration and thus a low equilibrium solubility in the host material [31]. As a result, if kinetics allow, implanted He atoms can precipitate as He gas bubbles, which grow to dimensions equivalent to that of the He^+-exposed region. This bubble formation can lead to significant morphological changes such as surface swelling at ion doses of over 10^{17} ions cm^{-2} [32, 33]. If all three characteristics are considered, implanted He^+ may accumulate significantly within nanostructures, leading to gas bubble growth and 'bloating' of targets without forming a steady-state radiation-damage profile. Simultaneously and unlike Ga^+, He^+ can scatter/diffuse and escape from irradiated targets into the surrounding vacuum by a process which we refer to as He^+ leakage. Consequently, He^+ may display a range of scattering behaviors in nanostructures resulting in both internal and surface damage to nanostructured targets (see figure S1 in the supplementary information, available online at stacks.iop.org/NANO/31/045302/mmedia).

Despite the physical understanding described above, details of the radiation effects due to FHIB have thus far only been investigated for a limited number of materials such as Si [32, 34, 35], Cu [32], Ni-Mo/Si [25], TiO_2 [34], and graphene [36], even though numerous other materials of interest exist. Diamond (crystalline carbon, hereafter referred to as c-C) is a particularly promising material in nanotechnology due to its extraordinary mechanical, optical, and thermal properties, and its biocompatibility [37–39] for micro- and nano-electromechanical systems [40, 41]. It is also of interest for quantum optics/computing [42, 43], magnetic resonance imaging (MRI) [44, 45], and as an electron-optical material in new microscopy techniques such as quantum electron microscopy [46]. Therefore, there is considerable interest in understanding how c-C can be probed and modified using

localized, targeted ion irradiation, for example a FHIB has been used to generate defects at controlled locations in diamond, which can subsequently be converted to luminescent nitrogen-vacancy centers for use in nanoscale MRI [27, 47].

In this work, we study the interaction of a FHIB with c-C nanostructures compared to those produced in crystalline silicon (hereafter referred to as c-Si). A new experimental approach to observe ion-nanostructure interactions in three dimensions (3D) is described, by preparing electron-transparent samples using FGIB and then characterizing FHIB-induced modifications in those samples both internally and externally by transmission and scanning electron microscopy (TEM and SEM), respectively. We investigated ion-nanostructure interactions as a function of material composition, ion dose, crystal orientation, substrate thickness, and ion energy. We observed nanostructure-specific physical phenomena, including anomalously long ion-penetration lengths and internal-gas-pressure-induced plastic deformation. We explain these phenomena by comparing material dimensions and morphologies measured by electron microscopy to Monte Carlo simulations. We used both SRIM [48] for ion-range prediction and irradiation of materials in 3D (IM3D) [49] to consider ion leakage effects in nanostructures. Furthermore, we have expanded our study to a new nanofabrication method for the production of 3D features through modification of existing micro- and nano-structures.

Method

Figure 1(a) outlines our experimental approach to investigate FHIB effects on nanostructures and describes the three-step experimental procedure graphically. First, we used FGIB milling to prepare monocrystalline nanostructures with different geometries and crystal orientations on a TEM grid. Second, we irradiated targeted regions of the nanostructures under various conditions with a FHIB. Finally, we use TEM and SEM to observe He^+-induced changes to internal and external morphologies, respectively. This method has advantages in that it provides direct 3D observation of site- and nanostructure-specific radiation damage without any post-processing of the specimens after ion irradiation. Previously, a similar method has been used, but no site- and nanostructure-specific damage was presented [50]. Using this experimental method, c-C nanostructures were the primary focus, while nanostructures of c-Si were chosen for comparison as there have already been a number of investigations of the response to c-Si to FHIB irradiation in both bulk and thin membrane forms [32, 51]. Throughout the text we use a number of variables to correlate material properties (geometry and composition) and ion exposure conditions to observed changes in the materials. We have summarized these variables in table 1. The supplementary material describes materials used, experiments, and measurements in greater detail.
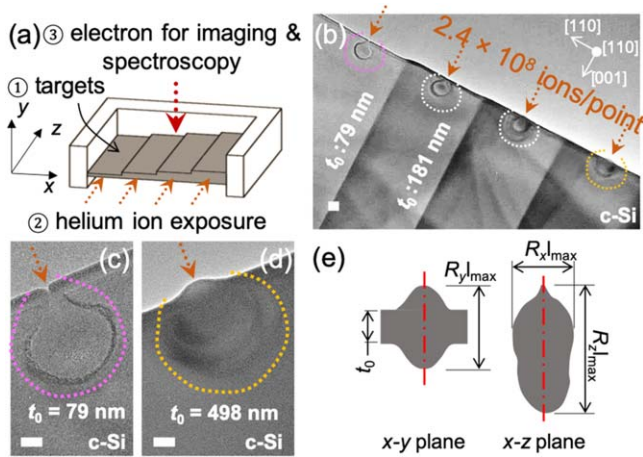
Figure 1. Experimental method and examples of ion-nanostructure interactions in silicon. (a) Schematic of experimental method and procedure. (1) Preparation of electron transparent targets with different geometries (gray color) by FGIB and lift-out technique. (2) Targeted irradiation of nanostructures. (3) Characterization by electron microscopy. (b) TEM image of c-Si membranes with different thicknesses irradiated with 35 keV He$^+$ as illustrated in (a). A point-exposure delivered 2.4×10^8 ions/point to each membrane in the direction of the orange arrows. (c), (d) Higher magnification TEM images when membrane thickness $t_0 = 79$ nm and $t_0 = 498$ nm in (b). The former shows removed volume and the latter shows swelled volume at the FHIB entry point as indicated by the orange arrows. (e) Measured parameters ($R_{x,y,z|\max}$) for He$^+$-exposed membranes viewed normal to the x–y plane (SEM) and the x–z plane (TEM). White scale bars represent a length of 100 nm.

Results and discussion

In this work, we studied interactions between a FHIB and c-C and c-Si nanostructures as a function of various parameters, including ion-exposure method (single point or scanned), exposure location, ion dose (D_0), ion energy (E_0), nanostructure geometry, and ion species. Figure 1 provides an overview of our approach and a summary of the damage observed in silicon samples for comparison to diamond in subsequent figures. In figures 1(b)–(d) we consider the interactions of a FHIB with c-Si membranes that were fabricated with different thicknesses (t_0). Comparing figures 1(c) and (d), we see significant surface swelling at the point where the FHIB enters the 498 nm thick membrane, which is absent from the 79 nm thick membrane. This comparison implies that FHIB-induced damage depends on sample geometry as is also seen in the case of c-C and discussed later in figure 5. Figure 1(e) shows how we measured FHIB-induced damage in a thin membrane using electron microscopy. The maximum lateral range of damage along the x-axis, termed $R_{x|\max}$ and longitudinal range along the z-axis, termed $R_{z|\max}$ was measured in the x–z plane, along with the maximum volume deformation along the y-axis in the x–y plane, $R_{y|\max}$. In a homogeneous medium, $R_{x|\max}$ and $R_{y|\max}$ are expected to be equal and would both be estimated as twice the radial distribution range R_r (measured from the optical axis), due to the axial symmetry of He$^+$ scattering in a bulk homogeneous solid. In our case, we must treat $R_{x|\max}$ and $R_{y|\max}$ differently, because damage is formed differently along the x- and y-axes.

Thus, $R_{x|\max}$ was comparable to $2R_r$ and $R_{y|\max}$ was used to estimate the observed volume deformation. We use these measured values as well as others listed in table 1 to explain results related to FHIB-induced damage in this work.

Figure 2 summarizes the observed interactions between a FHIB and c-C membranes. Figures 2(a), (b) show the surface of an 82 nm thick c-C membrane after irradiation by a linear scan with a FHIB at two different doses and shows that more FHIB-induced damage occurred along the x- and z-directions when a higher dose was applied. The observed swelling orthogonal to the beam direction was not always seen in previous reports [35], as it would have been destroyed during preparation of the TEM sample except in the case of the methods used in [3, 10]. Volumetric deformation seen in figures 2(a), (b) is indicative of dose-dependent FHIB-induced damage. Furthermore, comparison of these results with those for c-Si shown in figures 1(b)–(d) highlights the additional material dependence. Figure 2(c) is a magnified image of the yellow boxed region in figure 2(a) and shows that our method enables observation of changes in surface morphologies due to nanoscale sputtering. Figure 2(d) displays a TEM image of the damaged region within the nanostructure presented at the left side in figure 2(a). This figure shows the internal structure of the region irradiated by the FHIB, including longitudinal damage extending 634 nm below the surface. The depth of the longitudinal damage is larger than the 146 nm ion-penetration depth predicted by SRIM for 35 keV He$^+$ in c-C, which will be considered in further detail in discussions of figure 3. Figure 2(e) shows the results of electron energy-loss spectroscopy (EELS) analyses, where a shift in the energy of volume plasmon peak of c-C was observed and attributed to FHIB-induced damage. The volume plasmon energy depends on the density of the material and as such we used the shift in volume plasmon energy to estimate the change in density of the material due to interactions with the FHIB [52]. We estimated a density reduction of approximately 50% going from pristine c-C (3.47 g cm^{-3}) to damaged diamond (1.79 g cm^{-3}). The supplementary information describes how the estimation of density using EELS was conducted. Figures 2(f), (g) show the external structure of a 94 nm thick c-C membrane after a FHIB point exposure at the edge of the membrane. The longitudinal damage range observed is 938 nm, which is approximately 300 nm larger than the value shown in figure 2(d). This comparison implies that FHIB-induced morphology changes depend on exposure method and location. Figure 2(h) shows a TEM image of a 87 nm thick c-C membrane exposed to a 10 keV FHIB using a point-exposure at the center of the membrane. Strong surface sputtering was observed near the point where the FHIB entered the sample as He$^+$ loses more energy via nuclear interactions at 10 keV relative to 35 keV. Nuclear losses for 10 keV and 35 keV He$^+$ in c-C are 23.24 eV Å^{-1} and 10.43 eV Å^{-1}, respectively, as calculated by SRIM.

The results shown in figures 1 and 2 summarize the FHIB-induced damage in c-Si and c-C observed in this work and demonstrates that our method enables detailed observation of this damage. In the following sections, we will

Table 1. Summary of variables used in this work and the variables that they represent.

Variable	Definition
t_0	Membrane thickness
D_0	Ion dose
E_0	Kinetic energy of ion
R_r	Radial range of ion-induced damage in a homogeneous material
$R_{x|max}$, $R_{y|max}$, $R_{z|max}$	Maximum range of ion-induced damage along x, y and z axes. In a homogeneous material, $R_{x|max} = R_{y|max} = 2\,R_r$
$t_{d|max}$, $T_{d|max}$	$t_{d|max}$ represents the thickness of the deformed region i.e. $R_{y|max}$—t_0, which has a saturation value of $T_{d|max}$
P_{acc}, P_{acc}^{SRIM}, P_{acc}^{IM3D}	Probability of helium ion coming to rest inside the nanostructure (P_{acc}) as calculated by SRIM (P_{acc}^{SRIM}) or IM3D (P_{acc}^{IM3D})
P_{esc}	Probability of helium escaping from material i.e. $1 - P_{acc}$
pi, $pi|max$	Internal helium pressure within material ($_{pi}$) and maximum internal pressure at which higher order deformation proceeds
k	Deformation resistance factor

describe the results of targeted FHIB irradiation in c-Si and c-C nanostructures with respect to dose (D_0), membrane thickness (t_0), crystal orientation, and ion energy (E_0).

Figure 3 presents the results of our investigation of the effect of FHIB dose (D_0) and material (c-C versus c-Si) on FHIB-induced morphology changes using membranes having similar thicknesses (t_0). In order to study the effects of dose and composition, we prepared membranes from c-C and c-Si with t_0 of 73 nm and 71 nm, respectively. Each membrane used had the same crystal orientation ($\hat{x} = \hat{y} = [110]$ and $\hat{z} = [001]$). We performed a point-exposure with 35 keV He$^+$ at a central position on the membrane, normal to the x–y plane of each membrane, with five different values of D_0 (8.1×10^6, 4.1×10^7, 8.1×10^7, 1.6×10^8, and 2.4×10^8 ions/point), where each point has an effective focal area of about 1 nm^2.

Figures 3(a), (b) show representative results observed by TEM in c-C and c-Si, respectively ($D_0 = 2.4 \times 10^8$ ions/point). These images show the apparent boundary between damaged and undamaged regions in c-C and c-Si. Specifically, c-C exhibits an extended damage range along the z-axis ($R_{z|max} = 857$ nm) with three peaks in R_x observed moving along the z-axis and increased gas bubble formation, e.g. nanobubbles and clusters thereof, which we refer to as bubble clusters. In the case of c-Si, the damaged region shown in figure 3(b) is similar to the damaged region reported in previous studies with bulk c-Si substrates [33, 51]. However, in those works only nanobubbles were observed in c-Si even though the applied dose exceeded that required for bubble cluster formation (D_0 of 10^{17} ions cm^{-2}) [32]. We will discuss the reported absence of bubble clusters later in the text when we discuss ion leakage effects. Figures 3(c), (d) show SEM images of FHIB-exposed c-C and c-Si, respectively ($D_0 = 2.4 \times 10^8$ ions/point). These images show external damage in the form of volume deformation. Specifically, c-C exhibits extended damage with a measured $R_{y|max}$ value of 240 nm, which is 1.6 times larger than $R_{y|max}$ for c-Si. The increased gas bubble formation seen in c-C is likely to promote volume deformation as seen in previous reports for Si and Cu [32, 33, 53].

Figure 3(e) summarizes the observed trends in measured values of $R_{y|max}$ as a function of D_0 for c-C and c-Si. $R_{y|max}$ is larger for c-C than for c-Si and increases in both materials with D_0. The larger values of $R_{y|max}$ in c-C relative to c-Si are consistent with the larger lattice parameter in c-Si, which supports an increased probability of helium escape for c-Si, while the increase in $R_{y|max}$ with ion dose is expected based on the decrease in material density during damage formation and helium accumulation within the material. Figures S2–4 in the supplementary material show micrographs for other values of D_0. Figures 3(f), (g) summarize the evolution of damaged regions in the x–z plane as a function of D_0 with profiles of the damaged regions observed in TEM images of c-C and c-Si represented by solid colored lines. Figures 3(f), (g) also include three SRIM simulation results, He$^+$ distribution projected in the x–z plane, and densities of He$^+$ and vacancies along the z-axis. The supplementary material describes SRIM simulations in detail. Plotted densities of He$^+$ and vacancies were calculated using the minimum D_0 of 8.1×10^6 ions, because SRIM does not account for dynamic processes such as density reduction and gas bubble formation observed at higher doses [10, 48, 52]. Thus, comparison of experimental and simulation results is reasonable at doses of 8.1×10^6 ions where bubbles are not formed in both materials. The simulated He$^+$ distribution maps differ from experimental profiles in both c-C and c-Si. The simulated densities of He$^+$ and vacancies along the z-axis show only a single peak in both c-C and c-Si, while in experiments c-C exhibited multiple peaks. In figure 3(f), we describe the multiple peaks and valleys in the boundary between amorphous and crystalline material along the z-axis as separating Nth-order damaged regions. These labels will be used when discussing long-range ion propagation below. We determined the locations of peaks and valleys by observing the widest and narrowest $R_{x|max}$ values.

The material dependence of ion-induced damage and deformation observed is related to the thickness of the nanostructures. This dependence occurs because the calculated radial damage range (R_r) in each material is larger than half the membrane thickness $t_0/2 \cong 37$ nm, and so helium can escape from the material in a process that we term 'ion
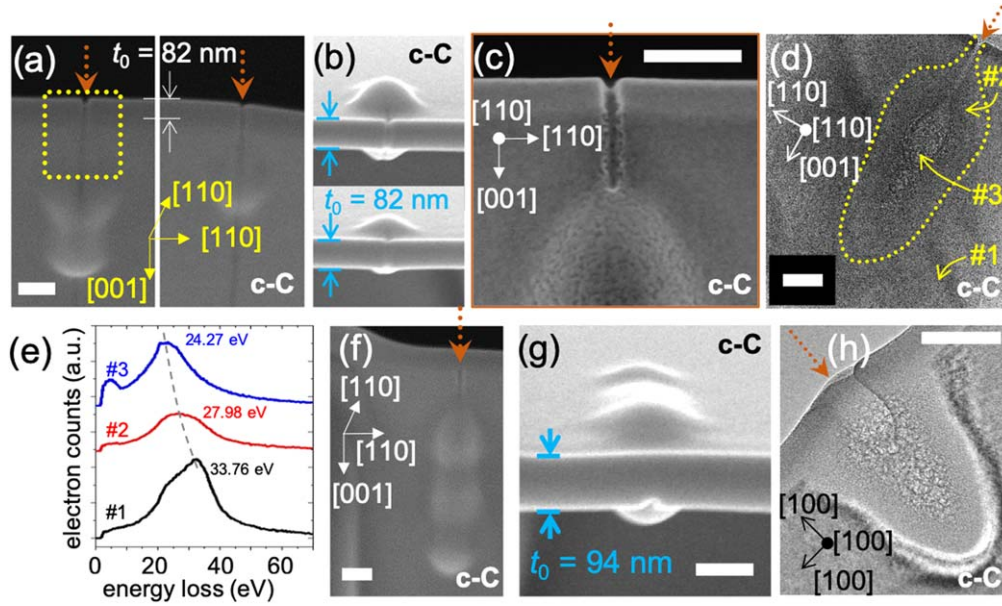
Figure 2. Examples of ion-nanostructure interactions in diamond (c-C). (a), (b) SEM images of 82 nm thick c-C membranes exposed to 35 keV He$^+$. A line-exposure along the *y*-axis delivered 2.4×10^8 (left) and 4.0×10^7 ions/line (right). Damage observed in (a) and (b) was viewed at angles of $52°$ and $-10°$, respectively, and shows dose-dependent volume deformation. (c) Magnified SEM image of region in yellow box in (a) shows a sputtered volume and a roughened surface. (d) TEM image of left side of sample in (a) showing internal He$^+$-induced damage within the region outlined by the dashed line. (e) EELS spectra showing the shift in energy of volume plasmon peaks, sampled from three points in (d). Peaks at 33.76, 27.98, and 24.28 eV in curves #1 to #3 resulted in calculated densities of 3.47, 2.38, and 1.79 g cm^{-3}. (f), (g) SEM images of 94 nm thick c-C membranes exposed to 35 keV He$^+$ with a dose of 2.4×10^8 ion/point and the same crystal orientation as in figures (a), (b). He$^+$ point-exposure was applied at the edge of the membrane on the *x–y* plane. Images show three volume deformations. (h) TEM image of 87 nm thick c-C membrane exposed to 10 keV He$^+$ with a dose of 8.0×10^7 ion/point. Surface sputtering and gas bubble formation are observed. White scale bars represent a length of 100 nm.

leakage'. The calculated values of R_r for c-C and c-Si using SRIM are 40.9 ± 21.5 nm and 145.3 ± 70.8 nm, respectively. Figures 3(f), (g) show the effect of membrane geometry by overlaying two gray-colored bars on simulation and experimental results representing membrane thickness. Inspection of the simulated He$^+$ distribution with respect to t_0 suggests that more He$^+$ scatters out of a virtual membrane in c-Si than in c-C, likely due to the reduced stopping power of 35 keV He$^+$ ions in c-Si (11.6 eV Å^{-1}) compared to c-C (29.8 eV Å^{-1}).

We quantified the number of He$^+$ ions coming to rest inside the membrane as the probability of He$^+$ accumulation (P_{acc}), where the probability of escape was $P_{esc} = 1 - P_{acc}$ for a given t_0. The resulting values calculated using SRIM $P_{acc}^{SRIM} = 0.73$ (c-C) and $P_{acc}^{SRIM} = 0.23$ (c-Si). This result indicates that the probability of He$^+$ trapping is 3.17 times larger in c-C than in c-Si due to larger loss of He$^+$ kinetic energy per collision in c-C (m_{He} is closer to m_C than m_{Si}). This trapping contributes not only to gas bubble nucleation, but also to subsequent collision cascades between incident primary ions and trapped helium, resulting in additional radiation damage in c-C, where the probability of ion leakage is lower than in c-Si. However, this SRIM calculation includes He$^+$ recoil back into the nanostructure, which cannot happen once the He$^+$ has left the film, as SRIM cannot handle real 3D geometries [54]. Thus, we performed a full 3D Monte Carlo simulation using IM3D, which accounts for the leakage of He$^+$ in arbitrary 3D geometries. The simulated

probabilities for accumulation using IM3D, P_{acc}^{IM3D}, were 0.69 and 0.08 in c-C and c-Si, respectively. Thus, the IM3D simulation results differ significantly from those obtained from SRIM.

Given the high P_{acc} in c-C, gas bubbles and atomic displacements are more probable in c-C than in c-Si. This increase in damage results in $R_{y|max}$ in c-C being 2.25 times larger than that in c-Si at the maximum D_0, as shown in figures 3(c)–(e). The supplementary material describes the calculation of P_{acc} and P_{esc} in detail. Figure S5 in the supplementary material shows P_{acc} as a function of t_0 for both c-C and c-Si.

The ion leakage effect enables us to explain the absence of bubble clusters in c-Si (figure 3(b)) at $D_0 = 2.4 \times 10^8$ ions/point, equivalent to 2.4×10^{22} ions cm^{-2}, since each point has an effective area of about 1 nm^2. This areal dose density is four and five orders of magnitude higher than the nucleation doses for nanobubbles and bubble clusters, respectively [32]. We would thus naively expect bubble clusters to form. By accounting for dose from the proximity effect and P_{acc}, the effective D_0 in figure 3(b) reduces to about 1.7×10^{17} ions cm^{-2} (SRIM) or 6.1×10^{16} ion cm^{-2} (IM3D). The effective D_0 obtained using IM3D is thus below the nanobubble nucleation dose of 10^{17} ions cm^{-2} reported in previous work [32]. While estimates of bubble nucleation dose thresholds are admittedly inexact, the fact that bubbles are indeed not observed does
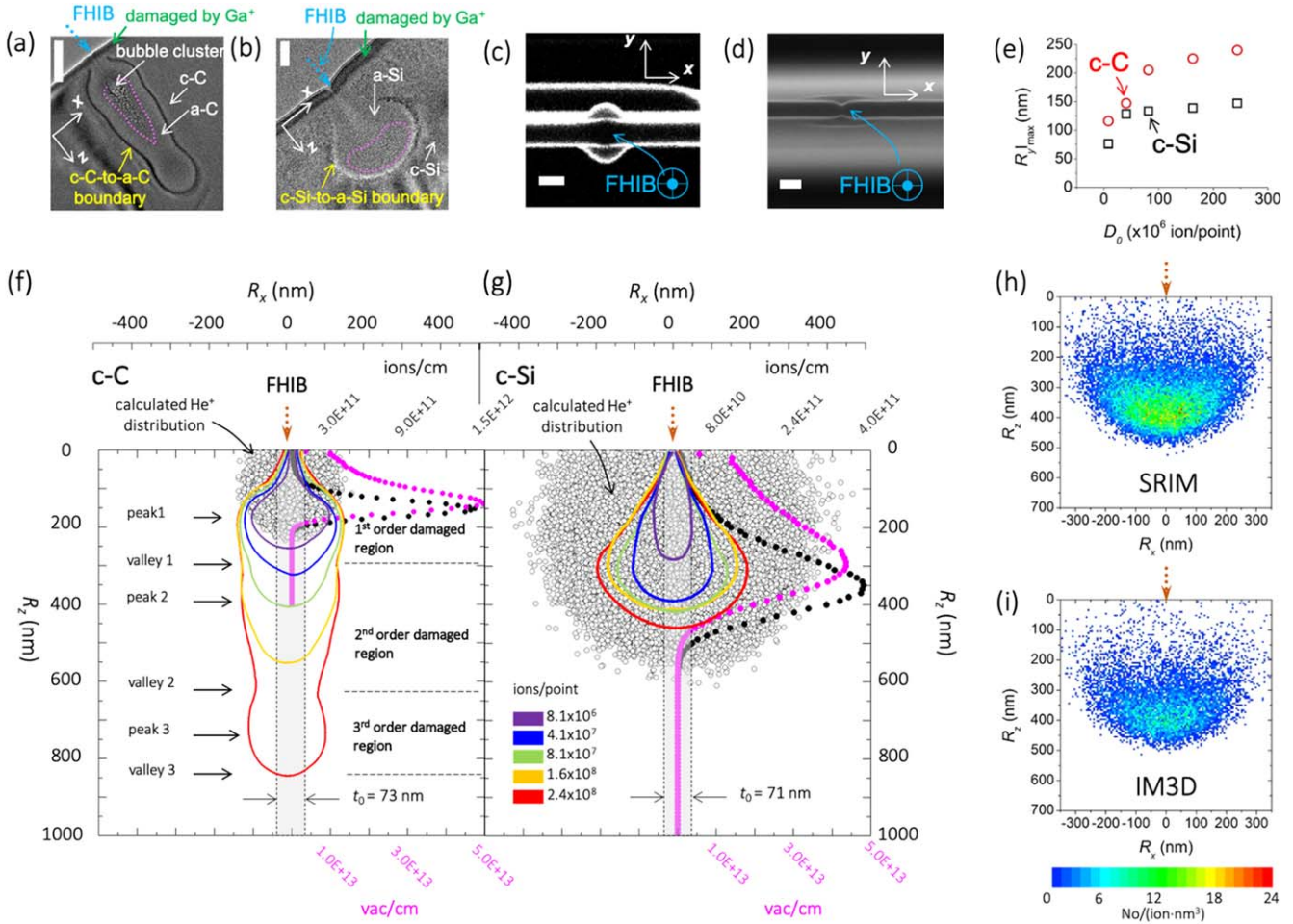
Figure 3. He$^+$-induced damage in c-C and c-Si as a function of D_0. White scale bars in (a)–(d) are 100 nm. (a), (b) TEM images of (x–z plane) He$^+$-exposed c-C membranes (a) and c-Si (b) (ion dose = 2.4×10^8 ions/point). The boundaries between crystalline and amorphous regions in c-C and c-Si are distinguishable. Measured $R_{z|max}$ for c-C and c-Si are 857 nm and 433 nm, respectively. Pink dotted lines in each figure show the boundary of regions where gas bubbles formed. (c), (d) SEM images of the surface morphology (x–y plane) of He$^+$-exposed c-C (c) and c-Si (d) membranes in the same samples as (a), (b). Measured $R_{y|max}$ for c-C and c-Si are 240 nm and 147 nm, respectively. (e) Measured $R_{y|max}$ for c-C and c-Si (x–y plane) as a function of D_0. (f), (g) Profiles of He$^+$-induced damage in c-C and c-Si (x–z plane) as a function of D_0, obtained from TEM images. Distribution of He$^+$ projected in the x–z plane, He$^+$ density (ions/cm) and vacancy density (vac/cm) along z-axis, calculated from SRIM are overlaid (black and magenta dots, respectively). The final locations of He$^+$ were projected onto the x–z plane. He$^+$ and vacancy densities were calculated using $D_0 = 8.0 \times 10^6$ ions/point. In c-C (f), three peaks and troughs in the width of the damaged region are observed moving along the z-axis (red trace) for $D_0 = 2.4 \times 10^8$ ions/point. Increasing numbers of peaks and troughs emerge with increasing dose. These peaks and troughs are used to define higher order damages regions as shown. Virtual membranes (y–z plane) with t_0 of 73 nm for c-C (f) and 71 nm for c-Si (g) are overlaid to show He$^+$ leakage due to the membrane geometry. (h), (i) 2D He$^+$ distribution on the x–z plane at the center of the y-axis in c-Si without (h) and with (i) consideration of finite membrane thickness ($t_0 = 73$ nm) using IM3D.

support the notion that IM3D describes ion-nanostructure interactions more accurately than SRIM.

Additionally, we provide an example of the necessity for consideration of He$^+$ leakage when computing ion-solid interactions, in figures 3(h), (i). The distributions calculated by SRIM (figure 3(h)) differ significantly from those calculated by IM3D (figure 3(i)). As IM3D accounts for the three-dimensional structure of the system, while SRIM does not, we presume figure 3(i) gives a more accurate estimate of the actual behavior of the process.

Figure 4 describes the evolution of long-range ion propagation in c-C as a function of D_0. The damaged region at the lowest D_0 of 8×10^6 ions/point in figure 4(a) does not include bubbles, which indicates that the $R_{y|max}$ measured in

figure 3(e) first occurred by a phase transition from c-C to amorphous carbon (a-C). We compare the vacancy density calculated in figure 3(f) with the threshold vacancy density of $(1–9) \times 10^{22}$ vac cm^{-3} required to convert c-C to a-C under broadband helium ion implantation [52, 55], due to the absence of existing experimental data using focused beams with c-C. Applying the proximity effect and P_{acc} corrections as before, the reduced vacancy densities are about 7.3×10^{22} vac cm^{-3} (SRIM) and 6.9×10^{22} vac cm^{-3} (IM3D). These values are consistent with the threshold vacancy density from the literature mentioned above.

The transition to an amorphous state not only leads to lower density, but also forms a geometric constraint at the interface between the amorphous and crystalline phases of the
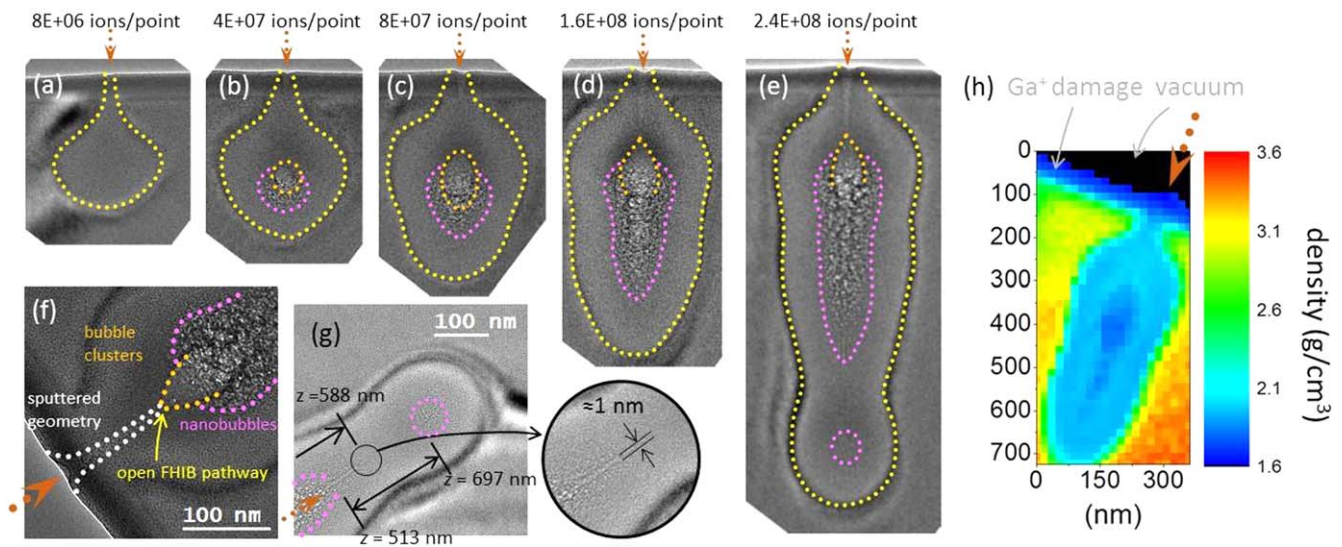
Figure 4. Evolution of long-range ion-propagation with increasing ion dose. TEM images in (a)–(e) were used to form the contours shown in figure 3(f). The dotted brown arrow indicates the direction of the incident FHIB. Yellow dashed lines, drawn by hand, mark the crystal-to-amorphous boundary in the material. This boundary forms a geometric constraint as explained in the text. (a) TEM image shows the damaged amorphous region without gas bubbles. (b) TEM image shows the onset of nucleation of nanobubbles (dashed pink line) and bubble clusters (dashed orange line). (c), (d) TEM images show the onset of the 2nd order damaged regions (as defined in figure 3(f)) with extended nanobubble formation along the z-axis. (e) TEM shows further extended He$^+$ propagation, resulting in a 3rd order damaged region ($R_{z|max} = 857$ nm). (f) TEM image shows the connection between the sputtered volume and bubble clusters, which act as an exit for helium gas and an entrance for the FHIB into the newly formed cavity. A white dotted line shows the geometric boundary of the sputtered volume. (g) Image shows a magnified view of a region 588 nm beneath the surface shown in figure 4(e). This image shows ultra-fine features with 1 nm lateral extent inside the membrane. (h) 2D density map, calculated using the volume plasmon energy measured by EELS. The specimen used here is shown in figure 2(a). The measured sample density had a range of 1.72–3.47 g cm^{-3}. The region where helium gas bubbles formed showed the lowest density values.

material where the rigid crystalline material constrains the ductile amorphous material. The yellow dashed line in figure 4(a) shows the boundary of the geometric constraint, which evolves with increasing He$^+$ irradiation dose as shown in figures 4(b)–(e). When the damaged amorphous region extends along the y-axis to the surface (i.e. when $t_0 < R_{y|max}$), the surface is readily deformed resulting in the observed 'bloating', an effect we take advantage of below as part of the 'blow forming' process. This bloating occurs because there is no longer a c-C layer at the surface acting as a geometrical constraint to the ductile amorphous material.

To establish the local material density in FHIB-irradiated c-C, we used EELS. The estimated average density in a-C (ρ_{a-C}) was 2.04 g cm^{-3} (figure S6), which indicates a 42% drop in density relative to c-C. This ρ_{a-C} of 2.04 g cm^{-3} is close to that expected for stable amorphous allotropes of carbon having densities of 2.06–2.35 g cm^{-3}, measured after ion implantation and micro-beam irradiation at 50–500 keV with various ion species [52, 55, 56]. The reduction in density also implies a drop in the elastic modulus and the material becomes more ductile as a-C is formed [55, 57].

It is also notable that the simulated He$^+$ distribution in c-C closely matched the observed damaged region in the experiment at the lowest D_0 of 8×10^6 ions/point, as shown in figure 3(f), presumably because the nucleation of gas bubbles did not occur and ion leakage in c-C was not significant.

Figures 4(b)–(e) show the formation and development of nanobubbles in c-C. Figure 4(b) shows the onset of both

nanobubbles and bubble clusters at D_0 of 4×10^6 ions/point. Above this dose, volume deformation is likely to be induced by gas bubble formation as the internal pressure, $_{pi}$, increases in the membrane (figures 4(c)–(e)). Figure 4(c) shows the growth of helium bubbles within a 1st order damaged region and at the onset of 2nd order damage. Figure 4(d) shows the continuation of those two processes with additional FHIB irradiation. The onset of 2nd order damage results from increased helium and vacancy accumulation deeper within the sample and thus greater helium penetration as scattering is reduced in the lower density material formed by accumulation of helium and vacancies. A region of 3rd order damage is observed in figure 4(e) at a dose of 2.4×10^8 ions/point. The 3rd order region is separated from the 2nd order region by a bubble-free region at $z = 513$ nm. The disappearance of nanobubbles in this region may be due to helium release, which can occur due to the rupture of deformed surfaces by high-pressure gas bubbles [53]. In this case, the helium gas may release through the entrance channel that formed due to sputtering and bubble clusters, as shown in figure 4(f). Therefore, He$^+$ can propagate through the formed internal cavity until it strikes sub-surface vacuum-carbon interfaces.

Figure 4(g) shows evidence of long-range FHIB propagation as a remnant of an ultra-fine FHIB (≈ 1 nm lateral width) is observed at $z = 588$ nm. This long-range FHIB propagation is likely responsible for creating the 3rd order volume deformation. The depth of field of FHIB is estimated to be ~ 1 μm based on the image resolution (1 nm) and the

beam convergence angle (1 mrad) [58], and supports this observation.

We have shown that FHIB exposure of c-C results in damage to the material and an associated decrease in material density. Here, we estimate changes in the density of FHIB-irradiated c-C membranes containing gas bubbles using EELS. Figure 4(h) shows a measured 2D density map with densities ranging from 1.72–3.47 g cm^{-3}. Based on the maximum density of a-C (2.95 g cm^{-3}) measured in [49], we divided the measured densities into two ranges: c-C for densities of 2.96–3.47 g cm^{-3} and a-C for 1.72–2.95 g cm^{-3}. Figures S7–S8 in the supplementary material shows more detailed density maps. Specifically, the density near nanoscale voids is lower than that expected for stable carbon allotropes (2.15–2.35 g cm^{-3}). A density of less than 2.15 g cm^{-3} supports plastic deformation in highly damaged regions (a-C) as observed in figures 2–4. A density less than that of stable allotropes caused by FHIB irradiation could occur due to tensile strain, which in turn leads to volume deformation, nanobubble formation, and transmission milling [51, 59]. These combined phenomena appear on the outer surface in figure 2(c). Additionally, secondary sputtering by scattered ions and sputtered C atoms inside the membrane may also play a role. EELS analysis also revealed a peak in the 4–8 eV energy-loss range for a-C (figures 2(e) and S9). This peak is associated with sp^2-hybridized carbon, shifting to lower energy and increasing in intensity with proximity to the path of the primary ion beam. Charged-particle beams have previously been used to convert sp^3 allotropes of carbon into sp^2 carbon, which is consistent with our observations [52, 60].

Figure 5 summarizes the results of our study of the effects of material thickness and ion energy on FHIB-induced damage in c-C. We considered two crystal orientations, $\hat{x} = \hat{y} = [110]$ and [100] in this work (crystal orientation was observed to have a negligible effect on the magnitude of deformation). Hereafter, each is referred to as c-C[110] and c-C[100]. A variety of values of t_0 ranging from 60 nm to 1 μm was considered for each crystal orientation. We define the deformed thickness $t_{d|\text{max}}$ for each membrane as the difference between $R_{y|\text{max}}$ and t_0. Most membranes were prepared from bulk c-C substrates, and some membranes were prepared on a TEM grid for subsequent analysis by TEM. A 35 keV FHIB was used to expose the center of samples with a fixed D_0 of 2.4×10^8 ions/point. Figures S10–13 show the collected micrographs for all relevant experimental results.

Figures 5(a)–(c) show the effect of t_0 on the deformation. Figure 5(a) shows the measured $t_{d|\text{max}}$ for c-C[110] and c-C [100] as a function of t_0, which clearly shows that $t_{d|\text{max}}$ depends on thickness, while crystal orientation has a negligible effect. Figure 5(b) shows SEM (top) and TEM (bottom) images in x–y and x–z planes for He$^+$-exposed c-C[100] for three different values of t_0. Figure 5(c) shows more experimental results of He$^+$-exposed c-C[100] inspected by SEM. As t_0 increases, figure 5(a) shows that the magnitude of deformation, $t_{d|\text{max}}$, first increases and then decreases, and figures 5(b), (c) shows that $R_{z|\text{max}}$ decreases monotonically.

The behavior of $t_{d|\text{max}}$ in figures 5(a)–(c) is presumably a consequence of the maximum internal pressure ($_{pi|\text{max}}$) that can build up inside membranes for the 1st order volume deformation before allowing higher order deformation. We define a deformation resistance factor k to determine $_{pi|\text{max}}$. The parameter k may have the same form of flexural rigidity for the case of a circular flat plate subjected to uniform pressure with a clamped edge [61]. This is valid if we assume that pressurized regions are constant as a circular shape in the x–y plane at the 1st order damage region and materials are homogeneous in all experiments. Then, k is simply a monotonically increasing function of t_0, because a thicker membrane will be more difficult to deform under a constant pressure. Consequently, we can summarize three important points as follows: (1) $_{pi|\text{max}}$ scales with k to a maximum value, which is equivalent to that of a bulk sample. (2) $_{pi}$ increases with the product of dose and the probability of helium accumulation ($D_0 \cdot P_{\text{acc}}$). (3) $t_{d|\text{max}}$ will reach a maximum deformation $T_{d|\text{max}}$ when $_{pi} = _{pi|\text{max}}$. Additional pressure above $_{pi|\text{max}}$ will contribute to the creation of higher order damage regions and volume deformation.

The quantitative estimation of k is not considered in this work for two reasons: (1) material properties of membranes change dynamically and are non-homogeneous, as shown in figure 4(h). (2) An increase in the surrounding volume of c-C relative to a-C produced by He$^+$ irradiation leads to different boundary conditions at each t_0. Specifically, when $t_0 \geqslant 2R_r$, a composite bi-layer will be formed consisting of a-C (interior) and c-C (exterior), which will lead to a change in mechanical properties, as the elastic modulus of c-C is of the order of ten times larger than that of a-C [57].

In summary, we can best explain the effect of thickness on $t_{d|\text{max}}$ by subdividing the thickness into three different regimes (see figure 5(a)) as follows. In the first regime, ($t_0 \leqslant 130$ nm), material deformation increases as t_0 increases. This increase is consistent with an increase in P_{acc} with increasing thickness. As t_0 increases, there is less helium leakage and more helium accumulates in the nanostructure resulting in greater deformation. In the second regime, where 130 nm $\leqslant t_0 \leqslant 375$ nm, $t_{d|\text{max}}$ decreases as t_0 increases. At larger value of t_0, the a-C region formed by the FHIB no longer extends all the way to the surface of the membrane along the y-axis. Consequently, a c-C layer exists at the surface that acts to constrain the ductile a-C and reduce deformation. This c-C layer increases in thickness as t_0 increases and thus reduces deformation. In the third regime where $t_0 \geqslant 375$ nm, no change in $t_{d|\text{max}}$ is observed at all. We interpret this as a micro-to-bulk transition, implying that the materials response to ion irradiation can be regarded as that of the bulk material ($k = 1$).

Unlike $t_{d|\text{max}}$, $R_{z|\text{max}}$ decreases monotonically with increasing t_0 before reaching a minimum at value when $t_0 > 375$ nm. This suggests that the reduction in material density along the ion-beam axis is lower in thicker samples for a given dose, which is consistent with an increase in k with increasing thickness. This implies that the rate of increase of k with respect to t_0 is larger than that of $D_0 \cdot P_{\text{acc}}$. If it were not, $R_{z|\text{max}}$ would follow the same trend as that of $t_{d|\text{max}}$ with increasing t_0. The rapid increase of k with t_0 implies that k is very small when $t_0 < 2 \cdot R_r$. This prediction is
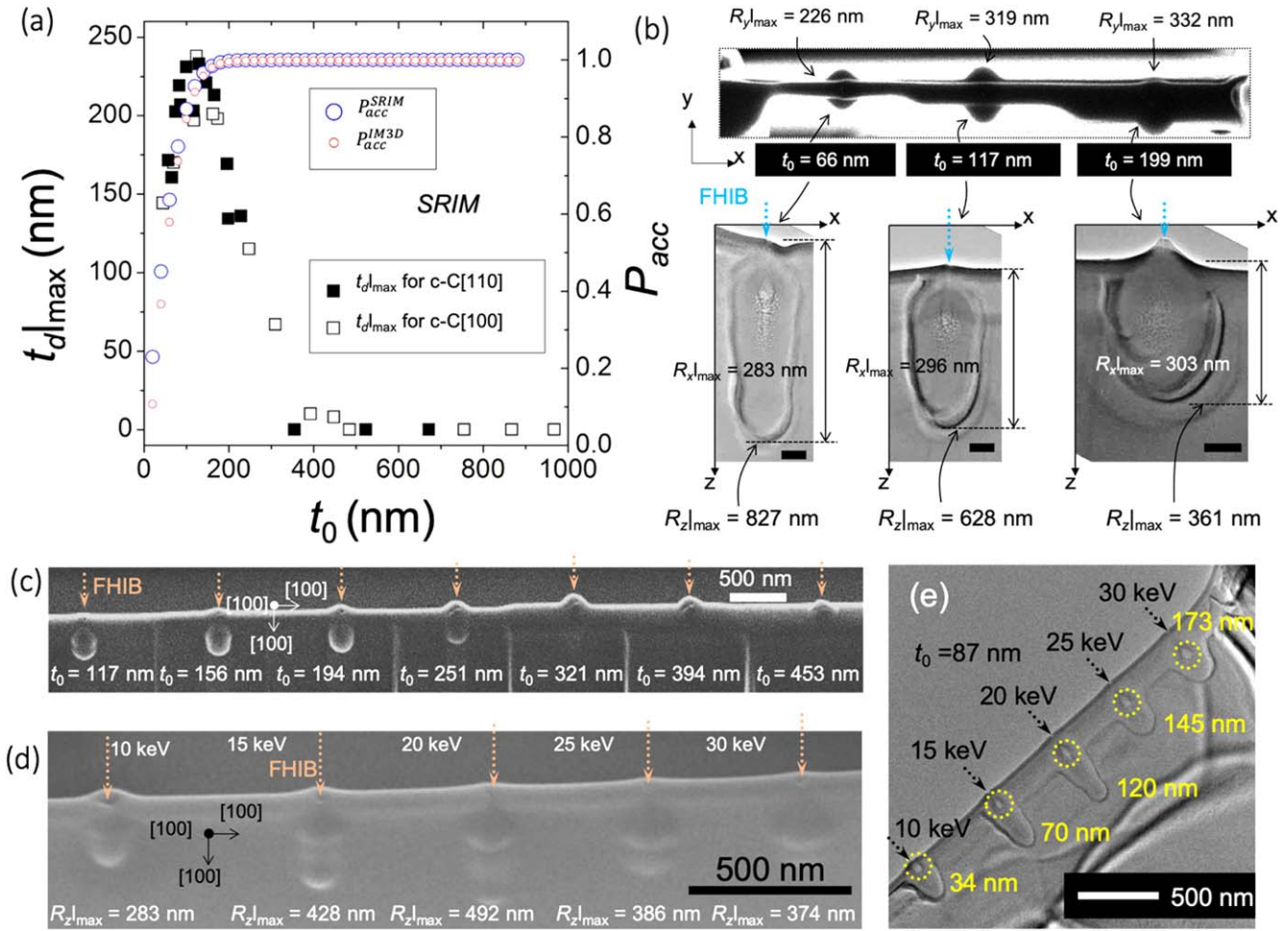
Figure 5. He$^+$-induced damage in c-C as a function of t_0 and E_0. All dotted arrows represent locations and directions of the incident FHIB. (a)–(c) Influence of He$^+$-induced damage as a function of t_0. A point exposure method was used to irradiate a point at the center of membranes with a 35 keV FHIB and D_0 of 2.4×10^8 ions/point. (a) We measured $t_{d|\text{max}}$ versus t_0. ■: $t_{d|\text{max}}$ of c-C[110], □: $t_{d|\text{max}}$ of c-C [100], and P_{acc}, calculated from SRIM(○) and IM3D(°), as a function of t_0 is overlaid. Both materials show similar changes in $t_{d|\text{max}}$, and t_0 has a significant effect on $t_{d|\text{max}}$. (b) Top: SEM image of exposed c-C[100] recorded normal to the x–y plane. Bottom: TEM images of exposed c-C[100] recorded normal to the x–z plane. Measured $R_{y|\text{max}}$ and $R_{z|\text{max}}$ for three different values of t_0 of 66, 117, and 199 nm are indicated. Both $R_{z|\text{max}}$ and gas bubble formation are reduced as t_0 increases. Black scale bars are 100 nm. (c) SEM image showing more test specimens exposed to He$^+$ as in (a), (b). Volume deformation along the z-axis decreases with t_0 and upward volume deformation dominates for $t_0 > 194$ nm. (d), (e) Influence of E_0 on He$^+$-induced damage. An 87 nm thick c-C[100] membrane was exposed with a fixed ion dose of 8×10^7 ions/point. SEM (d) and TEM (e) images show external and internal damage, respectively. In (e), dotted yellow circles and numbers represent locations of gas bubble clusters along the z-axis and their maximum lateral width, respectively. Damage appearing along the z-direction did not increase linearly with E_0.

reasonable because c-C membranes can be fully amorphized in the y–z plane for $t_0 < 2 \cdot R_r$. In fact, the longest $R_{z|\text{max}}$ of 827 nm was observed when $P_{acc} = 0.6125$ at $t_0 = 66$ nm. Additionally, when $t_0 > 130$ nm, volume deformation also occurred in an upward direction, as shown in figures 5(b), (c). This upward volume deformation is a result of deformation toward the weakest part of the FHIB-damaged area with stress concentration at the sputtered point of incidence of the FHIB. The upward volume deformation is typical of FHIB interactions with bulk materials [32, 33].

The measured $R_{x|\text{max}}$, $R_{y|\text{max}}$ and $R_{z|\text{max}}$ are similar for both crystal orientations studied. For instance, c-C[100] with t_0 of 66 nm exhibited $R_{x|\text{max}}$, $R_{y|\text{max}}$ and $R_{z|\text{max}}$ values of 266 nm, 226 nm, and 827 nm, respectively (figure 5(b)). These values are comparable to c-C[110] where t_0 was 73 nm

(figure 3(b)) and $R_{x|\text{max}}$, $R_{y|\text{max}}$ and $R_{z|\text{max}}$ were 272 nm, 240 nm, and 854 nm, respectively. The negligible effect of crystal orientation is likely related to the high He$^+$ dose, which collapses any anisotropy in mechanical properties and material density. In other words, a D_0 of 8.1×10^6 ions/point was sufficient to convert c-C to a-C, as shown in figure 4(a). The FHIB-induced conversion of c-C into amorphous carbon is likely to suppress ion channeling, which would exhibit a dependence on crystal orientation. Figure 5(a) also shows calculated P_{acc}^{SRIM} and P_{acc}^{IM3D} as a function of t_0. As t_0 increases, both values increased and are comparable with less than a 2% difference when $t_0 \geqslant 120$ nm.

In figures 5(d)–(e), we show the effect of beam energy on deformation. Figure 5(d) shows SEM and TEM micrographs, respectively, of c-C[100] membranes with thickness
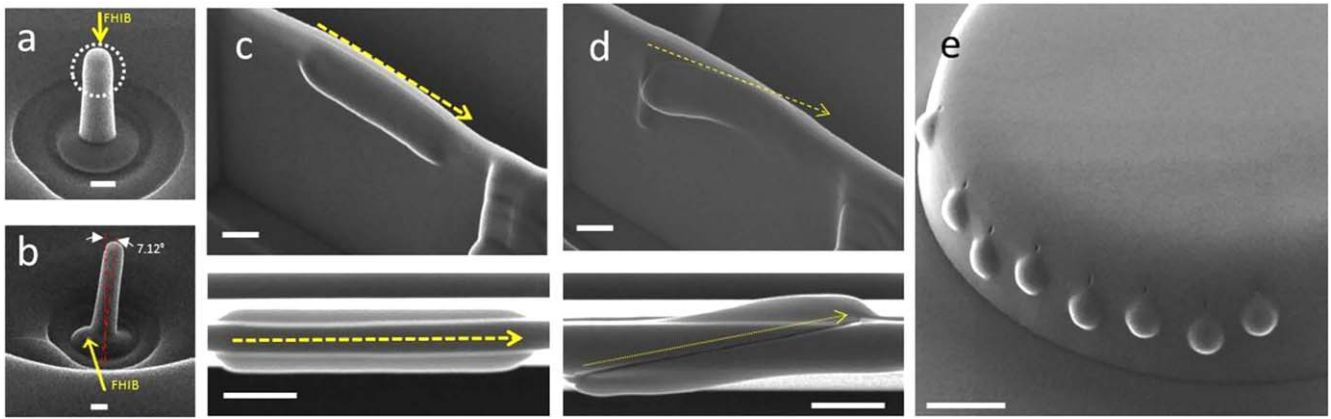
Figure 6. Control of nano-morphology via targeted ion irradiation of nanostructures; a nanoscale analogy to blow forming. (a) FHIB irradiation of a nano-pillar with a diameter of 100 nm. This image shows negligible deformation at the top of the pillar due to the absence of the geometric boundary. (b) FHIB irradiation at the boundary between a nano-pillar and its bulk substrate with a point exposure. The bulk substrate side forms a geometric constraint, which enabled deflection of the pillar in the opposite direction. In (a), (b), irradiation conditions were 2.4 pA ion current, $E_0 = 30$ keV and $D_0 = 8.0 \times 10^6$ ions/point. (c) Cylindrical geometry embedded in flat vertical membrane wall with a line-scan (top: tilt view at 45° and bottom: top view). (d) Asymmetric cylindrical geometry embedded in flat nano-wall with a diagonal line-scan. In (c), (d), the irradiation conditions were 2.4 pA ion current, $E_0 = 35$ keV and $D_0 = 8.0 \times 10^6$ ions/line. (e) Embedding nano-hemispheres in a micro-disk structure. A 35 keV FHIB was used to irradiate the edge of a micro-disk to form hemispheres at a regular interval. The depth variation with the same He^+ irradiation condition indicates not only the sensitivity of the location of exposed He^+ at the template structure but also the precision of the pre-patterned substrate.

$t_0 = 87$ nm implanted with different values of E_0 (see figure S16 for additional micrographs). Five different ion energies of 10, 15, 20, 25, and 30 keV were used with a fixed D_0 of 8×10^7 ions/point. As E_0 increases, the locations of bubble clusters shifted further away from the membrane edge along the z-axis and upward surface swelling was reduced. The shift in the location of bubbles can be explained by the increased He^+ penetration depth with increasing E_0. Correspondingly, peak locations of densities of He^+ and vacancies in the longitudinal direction shift deeper [11, 32].

In contrast to the monotonic shift in bubble location, $R_{z|\max}$ did not show a monotonic increase with E_0, instead decreasing from 492 to 386 nm as E_0 increased from 20 to 25 keV. The origin of this change in $R_{z|\max}$ with ion energy may be related to the following three physical processes as E_0 increases (see figures S17–19 for supporting data): (1) the ratio of electronic to nuclear stopping power decreases, resulting in increased simulated $R_{x,y,z}$ and a decrease in simulated sputter yield. (2) Densities and peak locations of He^+ and vacancies in the longitudinal direction decrease and increase, respectively. This fact implies that not only is greater delivery of He^+ required to coalesce nanobubbles into bubble clusters, but also larger bubbles are likely to be created. The dashed yellow circle in figure 5(e) shows that the maximum lateral width of bubble clusters increases as E_0 increases. (3) At a given $t_0 = 87$ nm, the probability of helium accumulation (P_{acc}) decreases, implying less damage. As E_0 increases, $R_{x,y,z}$ increases and the density of He^+ and P_{acc} decrease. Comparing these three processes with experimental results, we can explain the nonlinearity as follows: the change in $R_{z|\max}$ follows the tendency of the first process when $E_0 < 25$ keV. This is presumably due to reduced significance of P_{acc}, because most of the incident ions reside inside the membranes, *i.e.* P_{acc}^{SRIM} and P_{acc}^{IM3D} are over 0.92 and

0.88 when $E_0 < 20$ keV. The change in $R_{z|\max}$ follows tendencies of the second and third processes when $E_0 > 25$ keV. In this case, P_{acc} decreases abruptly from 0.92 to 0.81 (P_{acc}^{SRIM}) and from 0.88 to 0.78 (P_{acc}^{IM3D}), respectively. Furthermore, the density of He^+ reduces. Thus, more ions are required to reach the dose for nanobubble/bubble cluster nucleation, which is the key to promoting long-range ion-propagation, as stated previously in discussions of figures 4(b)–(e). Thus, we concluded that an E_0 of 20 keV efficiently formed gas bubbles with the combination of intermediate values of P_{acc}, $R_{x,y,z}$, and He^+ density, resulting in the longest $R_{z|\max}$ in figure 5(d).

Figure 6 shows advanced control of morphology by targeted He^+ irradiation of nanostructures, which formed different geometric constraints. In the results described so far, we observed nano-spherical volume deformation on membrane walls, which is the result of internal gas pressure balanced by the constraining force of the material surface. Further, we confirmed that this volume deformation is dependent on D_0, t_0, E_0, and location in c-C, implying that we can control the volume deformation deterministically by controlling these parameters with the help of the geometric constraint provided by a controlled target. We interpreted our results as a nanoscale analogy to blow forming [62] induced by helium pressure inside and surrounding existing micro- and nano-targets.

Figure 6(a) shows minimal volume deformation formed in a nanopillar in contrast to the case when $t_0 = 100$ nm, which resulted in $t_{d|\max}$ of 230 nm as in figure 5(a). This minimal volume deformation in the nanopillar is due to the absence of geometrical constraint and the high P_{esc}^{IM3D} of 0.40 in the pillar geometry. Figure 6(b) shows the use of geometrical constraint by FHIB irradiation at the boundary between a pillar and a bulk substrate, which acts as the geometrical constraint. We could deflect the nanopillar in a direction

opposite to where $_{pi}$ formed at the boundary. Furthermore, we also formed larger and more complex features in order to show the nanofabrication capabilities of He$^+$-assisted blow forming.

Figures 6(c), (d) show the results of He$^+$ irradiation of a membrane with two different line-scan directions. Figure 6(c) shows the cylindrical geometry of a nanocavity with uniform volume deformation in the *y*-axis along the *x*-axis. In this case, a geometric constraint formed uniformly along the *x*-direction because we fixed the *y*-position of the FHIB at the centerline of the membrane. Figure 6(d) shows an example of using the line-scan in a diagonal direction on top of the membrane. As the FHIB moves diagonally, the geometrical constraint changes, resulting in an asymmetric cylindrical geometry formed in the membrane.

Figure 6(e) shows an example of using the point-exposure in a micro-disk fabricated by FGIB. We performed the FHIB irradiation along the edge of the micro-disk of radius 5.50 μm, but with two slightly different radial locations of about 5.50 and 5.53 μm. The different locations effectively formed different geometric constraints due to the limitation of shaping a 90° vertical wall based on the Gaussian tail of FGIB. Consequently, the FHIB formed hemispheres in slightly different vertical locations. This example shows a novel application of the FHIB to produce localized features in large patterns.

Conclusions

Targeted ion irradiation of nanostructures has been shown to be an effective method for nanoscale modification of materials via a combination of radiation damage, helium implantation, and phase transition leading to different material properties in the deformation region. Our method offers the unique capabilities of observing site- and nanostructure-specific damage induced by targeted ion irradiation. We also present new He$^+$-induced damage in nanostructures of c-C and c-Si that have not previously been reported. Specifically, the FHIB irradiation of c-C nanostructures exhibited extended damage due to long-range ion propagation and plastic deformation. Our study revealed that the extended damage was the result of dynamic changes associated with stopping power, phase transition, mass density, bubble nucleation/growth, and helium leakage. We have explained the role of material, ion dose, crystal orientation, dimension (thickness), and ion energy in nanostructure-specific He$^+$-induced damage using electron microscopy and spectroscopy, and Monte Carlo simulations using SRIM and IM3D. Additionally, we have shown radiation damage in nanostructures to be influenced by other irradiation conditions, such as ion species, exposure method, and location. We have also demonstrated the deterministic control of morphologies at the nanoscale via targeted He$^+$ irradiation in existing micro- and nano-structures.

Although our investigation showed many advantages in the observation of He$^+$-induced morphological changes, a full understanding of He$^+$ interaction with nanostructures is still limited by a number of dynamic changes in materials properties. These are dependent on geometry and difficult to quantitatively predict, such as density of deposited helium and changes in elastic modulus following amorphization. However, we anticipate that our method and results will enable new ways to investigate materials physics, locally functionalize materials, and fabricate nanostructures. Our results can potentially be used to manipulate the hardest material, diamond, locally for micro- and nano- electro-mechanical systems [57].

ORCID iDs

Richard G Hobbs ⬤ https://orcid.org/0000-0003-0855-3710
Akshay Agarwal ⬤ https://orcid.org/0000-0002-5944-3346
Karl K Berggren ⬤ https://orcid.org/0000-0001-7453-9031

References

[1] Hedler A, Klaumünzer S L and Wesch W 2004 *Nat. Mater.* **3** 804
[2] Moon M-W, Lee S H, Sun J-Y, Oh K H, Vaziri A and Hutchinson J W 2007 *Proc. Natl Acad. Sci. USA* **104** 1130
[3] Liontas R, Gu X W, Fu E, Wang Y, Li N, Mara N and Greer J R 2014 *Nano Lett.* **14** 5176
[4] Kumar N, Kumar R, Kumar S and Chakarvarti S K 2016 *Radiat. Phys. Chem.* **119** 44
[5] Shang L Y, Zhang D and Liu B Y 2016 *Physica* E **81** 315
[6] Ronning C *et al* 2010 *Phys. Status Solidi* b **247** 2329
[7] Hoffmann S, Bauer J, Ronning C, Stelzner T, Michler J, Ballif C, Sivakov V and Christiansen S H 2009 *Nano Lett.* **9** 1341
[8] Möller W, Johannes A and Ronning C 2016 *Nanotechnology* **27** 175301

[9] Willke P, Amani J A, Sinterhauf A, Thakur S, Kotzott T, Druga T, Maiti K, Hofsass H and Wenderoth M 2015 *Nano Lett.* **15** 5110

[10] Johannes A, Noack S, Wesch W, Glaser M, Lugstein A and Ronning C 2015 *Nano Lett.* **15** 3800

[11] Arora W J, Sijbrandij S, Stern L, Notte J, Smith H I and Barbastathis G 2007 *J. Vac. Sci. Technol.* B **25** 2184

[12] Flatabo R, Agarwal A, Hobbs R, Greve M M, Holst B and Berggren K K 2018 *Nanotechnology* **29** 275301

[13] Guo Q, Landau P, Hosemann P, Wang Y and Greer J R 2013 *Small* **9** 691

[14] Vuuren A J V, Skuratov V A, Uglov V V, Neethling J H and Zlotski S V 2013 *J. Nucl. Mater.* **442** 507

[15] Ding M-S, Du J-P, Wan L, Ogata S, Tian L, Ma E, Han W-Z, Li J and Shan Z-W 2016 *Nano Lett.* **16** 4118

[16] Jung Y J, Homma Y, Vajtai R, Kobayashi Y, Ogino T and Ajayan P M 2004 *Nano Lett.* **4** 1109

[17] Robinson A P, Burnell G, Sahonta S-L and MacManus-Driscoll J 2009 *Adv. Eng. Mater.* **11** 907

[18] Economou N P, Notte J A and Thompson W B 2012 *Scanning* **34** 83

[19] Winston D *et al* 2009 *J. Vac. Sci. Technol.* B **27** 2702

[20] Postek M T, Vladar A, Archie C and Ming B 2011 *Meas. Sci. Technol.* **22** 024004

[21] Joens M S *et al* 2013 *Sci. Rep.* **3** 3514

[22] Scholder O, Jefimovs K, Shorubalko I, Hafner C, Sennhauser U and Bona G-L 2013 *Nanotechnology* **24** 395301

[23] Yang J, Ferranti D C, Stern L, Sanford C A, Huang J, Ren Z, Qin L-C and Hall A R 2011 *Nanotechnology* **22** 285310

[24] Fox D S *et al* 2015 *Nano Lett.* **15** 5307

[25] Gonzalez C M *et al* 2014 *J. Vac. Sci. Technol.* B **32** 021602

[26] Wu H, Stern L A, Xia D, Ferranti D, Thompson B, Klein K L, Gonzalez C M and Rack P D 2014 *J. Mater. Sci., Mater. Electron.* **25** 587

[27] Huang Z, Li W-D, Santori C, Acosta V M, Faraon A, Ishikawa T, Wu W, Winston D, Williams R S and Beausoleil R G 2013 *Appl. Phys. Lett.* **103** 081906

[28] Cybart S A, Cho E Y, Wong T J, Wehlin B H, Ma M K, Huynh C and Dynes R C 2015 *Nat. Nanotechnol.* **10** 598

[29] Stanford M G *et al* 2016 *Sci. Rep.* **6** 27276

[30] Giannuzzi L A, Prenitzer B I and Kempshall B W 2005 *Introduction to Focused Ion Beams* ed L A Giannuzzi and F A Stevie (Dordrecht: Kluwer Academic Publishers) pp 13–52

[31] Kashinath A and Demkowicz M J 2011 *Modelling Simul. Mater. Sci. Eng.* **19** 035007

[32] Livengood R, Tan S, Greenzweig Y, Notte J and McVey S 2009 *J. Vac. Sci. Technol.* B **27** 3244

[33] Stanford M G, Lewis B B, Iberi V, Fowlkes J D, Tan S, Livengood R and Rack P D 2016 *Small* **12** 1779

[34] Fox D, Chen Y, Faulkner C C and Zhang H 2012 *Beilstein J. Nanotechnol.* **3** 579

[35] Li R, Zhu R, Chen S, He C, Li M, Zhang J, Gao P, Liao Z and Xu J 2019 *J. Vac. Sci. Technol.* B **37** 031804

[36] Hang S, Moktadir Z and Mizuta H 2014 *Carbon* **72** 233

[37] Fairchild B A *et al* 2008 *Adv. Mater.* **20** 4793

[38] Sumant A V, Auciello O, Liao M and Williams O A 2014 *MRS Bull.* **39** 511

[39] Hausmann B J M, Bulu I, Venkataraman V, Deotare P and Loncar M 2014 *Nat. Photon.* **8** 369

[40] Zalalutdinov M K, Ray M P, Photiadis D M, Robinson J T, Baldwin W J, Butler J E, Feygelson T I, Pate B B and Houston B H 2011 *Nano Lett.* **11** 4304

[41] Kohn E, Gluche P and Adamschik M 1999 *Diam. Relat. Mater.* **8** 934

[42] Santori C, Barclay P E, Fu K-M C, Beausoleil R G, Spillane S and Fisch M 2010 *Nanotechnology* **21** 274008

[43] Chu Y *et al* 2014 *Nano Lett.* **14** 1982

[44] Rugar D, Mamin H J, Sherwood M H, Kim M, Rettner C T, Ohno K and Awschalom D D 2014 *Nat. Nanotechnol.* **10** 120

[45] Bhallamudi V P and Hammel P C 2015 *Nat. Nanotechnol.* **10** 104

[46] Kruit P *et al* 2016 *Ultramicroscopy* **164** 31

[47] McCloskey D, Fox D, O'Hara N, Usov V, Scanlan D, McEvoy N, Duesberg G S, Cross G L W, Zhang H Z and Donegan J F 2014 *Appl. Phys. Lett.* **104** 031109

[48] Ziegler J F, Ziegler M D and Biersack J P 2010 *Nucl. Instrum. Methods Phys. Res.* B **268** 1818–23

[49] Li Y G, Yang Y, Short M P, Ding Z J, Zeng Z and Li J 2015 *Sci. Rep.* **5** 18130

[50] Reutov V F and Sokhatskiĭ A S 2003 *Tech. Phys.* **48** 68

[51] Tan S, Klein K, Shima D, Livengood R, Mutunga E and Vladár A 2014 *J. Vac. Sci. Technol.* B **32** 06FA01

[52] Fairchild B A, Rubanov S, Lau D W M, Robinson M, Suarez-Martinez I, Marks N, Greentree A D, McCulloch D and Prawer S 2012 *Adv. Mater.* **24** 2024

[53] Evans J H 1977 *J. Nucl. Mater.* **68** 129

[54] Yang Y, Li Y G, Short M P, Kim C-S, Berggren K K and Li J 2018 *Nanoscale* **10** 1598

[55] Khmelnitsky R A, Dravin V A, Tal A A, Zavedeev E V, Khomich A A, Khomich A V, Alekseev A A and Terentiev S A 2015 *J. Mater. Res.* **30** 1583

[56] Bosia F, Argiolas N, Bazzan M, Fairchild B A, Greentree A D, Lau D W M, Olivero P, Picollo F, Rubanov S and Prawer S 2013 *J. Phys.: Condens. Matter* **25** 385403

[57] Battiato A *et al* 2016 *Acta Mater.* **116** 95

[58] Hlawacek G, Veligura V, van Gastel R and Poelsema B 2014 *J. Vac. Sci. Technol.* B **32** 020801

[59] Marshall M M, Yang J and Hall A R 2012 *Scanning* **34** 101

[60] Duan H, Xie E, Han L and Xu Z 2008 *Adv. Mater.* **20** 3284

[61] Timoshenko S and Woinowsky-Krieger S *Theory of Plates and Shells* 2nd edn (New York: McGraw-Hill)

[62] Ding S, Liu Y, Li Y, Liu Z, Sohn S, Walker F J and Schroers J 2014 *Nat. Mater.* **13** 494

Supporting Material for

Focused-Helium-Ion-Beam Blow Forming of Nanostructures: Radiation Damage and Nanofabrication

Chung-Soo Kim[1*], Richard G Hobbs[2*], Akshay Agarwal[1], Yang Yang[3], Vitor R Manfrinato[1], Michael P Short[3], Ju Li[3,4] and Karl K Berggren[1]

[1]Research Laboratory of Electronics, Massachusetts Institute of Technology, Cambridge, Massachusetts, 02139, United States

[2]School of Chemistry, Advanced Materials and Bioengineering Research (AMBER) Centre and Centre for Research in Adaptive Nanostructures and Nanodevices (CRANN), Trinity College Dublin, Ireland

[3]Department of Nuclear Science and Engineering, Massachusetts Institute of Technology, Cambridge, Massachusetts, 02139, United States

[4]Department of Materials Science and Engineering, Massachusetts Institute of Technology, Cambridge, Massachusetts, 02139, United States

1. Materials, experiments and measurements

Materials: We used monocrystalline silicon (c-Si) and diamond (c-C). The c-Si was prepared from a transmission electron microscope (TEM) grid, supplied from Hitachi High-Tech Science Corporation). The c-C we used was chemical-vapor-deposition grown c-C plates ((100), P2, item number: 145-500-0253) supplied from Element Six. This c-C plate has a Boron and Nitrogen concentration of <0.05 ppm and <1 ppm, respectively.

Preparation of nanostructures: Nanostructured c-Si and c-C membranes were prepared by using a focused ion beam/scanning electron microscope (FIB/SEM) dual beam system (Helios Nanolab 600, FEI Company). The TEM grid form of c-Si simplified our experiment, because it did not

require the lift-out process. Nanostructures of c-C were prepared using the lift-out process using a micro-probe system (OMNI probe) as c-C was supplied as a bulk c-C plate. A 30 keV focused gallium ion beam (FGIB) was used to make thin membranes. We used 30 keV in order to fabricate membranes of uniform thickness, because low energy ion milling can degrade the uniformity of the membrane (even though it can reduce the thickness of the gallium-implanted layer at the surface of FGIB fabricated membranes). The use of FIB enabled us to fabricate different geometries of nanostructures.

Targeted ion irradiation: A focused helium ion beam (FHIB) was obtained using a helium ion microscope (HIM) (Orion Plus, Carl Zeiss Ltd). The probe current used ranged from 0.9 pA to 1.2 pA, depending on instrument condition. We used a constant working distance of 7 mm for all irradiation experiments.

Damage characterization: We observed external damage using SEM (Helios Nanolab 600) and HIM (Orion Plus). We observed internal damage using TEM (JEOL 2010F and 2010HR) at an energy of 100 kV. We estimated the change in density in nanostructures by electron-energy-loss spectroscopy (EELS) on the JEOL 2010F. In EELS, the shift in volume plasmon energy corresponds to a shift in mass density, which enabled us to estimate the density of nanostructures. The volume plasmon energy (E_p) in the *Drude* model is given by $E_p = \hbar \sqrt{e^2 n / m \varepsilon_0}$ where $\hbar$ is the reduced Planck's constant; e is the elementary charge; n is the volumetric electron density; m is the electron mass (we chose m = 0.87 m_0, where m_0 is the electron mass at rest, and proportionality constant was found to be a fitting constant valid for diamond-like carbon[1]), and ε_0 is the dielectric constant in vacuum. Alternatively, the bulk plasmon energy can be expressed by $E_p = (28.82\ eV)\sqrt{z\rho/A}$, where z is the number of free (valence) electrons per atom, A is the atomic weight, and ρ is the volumetric density (g/cm^3).

Monte Carlo simulation: We used stopping range in ion with matters (SRIM) in order to calculate the stopping power (electronic stopping power, nuclear stopping power, and the sum of two) and range distribution and damage distribution.[2] We used the "detailed calculation with full damage cascades" method with input mass densities of 3.515 g/cm^3 and 2.329 g/cm^3 for diamond and silicon, respectively. we used default values of lattice binding energy, surface binding energy and displacement energy. The number of ions used for the calculation was 100,000. Here, we also calculated the probability of He$^+$ accumulation (P_{acc}) and of escape ($P_{esc} = 1 - P_{acc}$) in order to consider the nanostructures' geometric effects. In order to calculate P_{acc} and P_{esc}, we used SRIM output file of Range_3D.txt. Depth X, Lateral Y and Lateral Z in the SRIM output were Z, X, and Y coordinate in our study. Using the y-axis coordinate, we counted the number of He$^+$ in the range $-t_0/2 \leq y \leq t_0/2$. This gave us the probability of He$^+$ accumulation (P_{acc}), and thus of escape ($P_{esc} = 1 - P_{acc}$). The SRIM calculation for geometric effects has a limitation for considering the ion leakage effect. In SRIM, artificial He$^+$ recoiled back into the nanostructure induces calculation errors in P_{acc} and P_{esc}. Thus, we also performed 3D Monte Carlo simulation using an Irradiation of Materials in 3D (IM3D).[3] IM3D can consider the effect of nanostructured geometry, thus, it can consider the ion leakage effect accurately compared to the SRIM. Simulation parameters in SRIM and IM3D were the same.

2. Ion dose and vacancy density corrections for point-exposure scheme

Ion dose of 2.4×10^8 ions/point delivered *via* point-exposure is equivalent to an areal dose of 2.4×10^{22} ions/cm^2 with the assumption that the exposed area is 1 nm^2, which is reasonable given the beam width of FHIB observed in our study was approximately 1 nm. This areal dose is four

and five orders of magnitude higher than the threshold doses for the nucleation of nanobubbles and bubble clusters, respectively.[4] These nucleation doses were estimated using areal-exposure, thus, He^+ distribution overlaps with this exposure scheme. This overlap can be treated as the proximity effect. Therefore, D_0 with the point-exposure can be lessened by proximity by a factor given by $(0.5 \cdot R_{x|max}/\text{pixel size})^2$, which is equal to 180^2, compared to the areal-exposure. Here, we assumed a pixel size of 1 nm. By considering the proximity effect with probability of accumulated He^+ (P_{acc}), the effective ion dose is likely to be reduced to about 1.7×10^{17} ion/cm^2 (SRIM) or 6.1×10^{16} ion/cm^2 (IM3D). The newly-estimated ion dose using IM3D is closer to nanobubble nucleation dose of 10^{17} ion/cm^2, reported in previous work.[4]

We applied the same rule of correction using the proximity effect and P_{acc} in order to estimate the vacancy density induced by point-exposure. First, we multiplied the vacancy density in Figure 2f by 10^{14} cm^2 to convert from vac/cm to vac/cm^3 (assuming a 1 nm^2 FHIB spot-size as before). The calculated volume vacancy density of 10^{27} vac/cm^3 even with the lowest D_0 is four orders of magnitude higher than the threshold vacancy density in c-C. Applying the proximity effect (a factor of about 100^2) and P_{acc} corrections (e.g., $P_{acc}^{SRIM} = 0.73$ and $P_{acc}^{IM3D} = 0.69$) as before, the reduced vacancy densities are about 7.3×10^{22} vac/cm^3 (SRIM) and 6.9×10^{22} vac/cm^3 (IM3D). These values are now consistent with the known threshold vacancy density of 1-9×10^{22} vac/cm^3 required to convert c-C to a-C under ion implantation,[5,6] due to the absence of existing experimental data using FHIB with c-C.

3. Supplementary figures
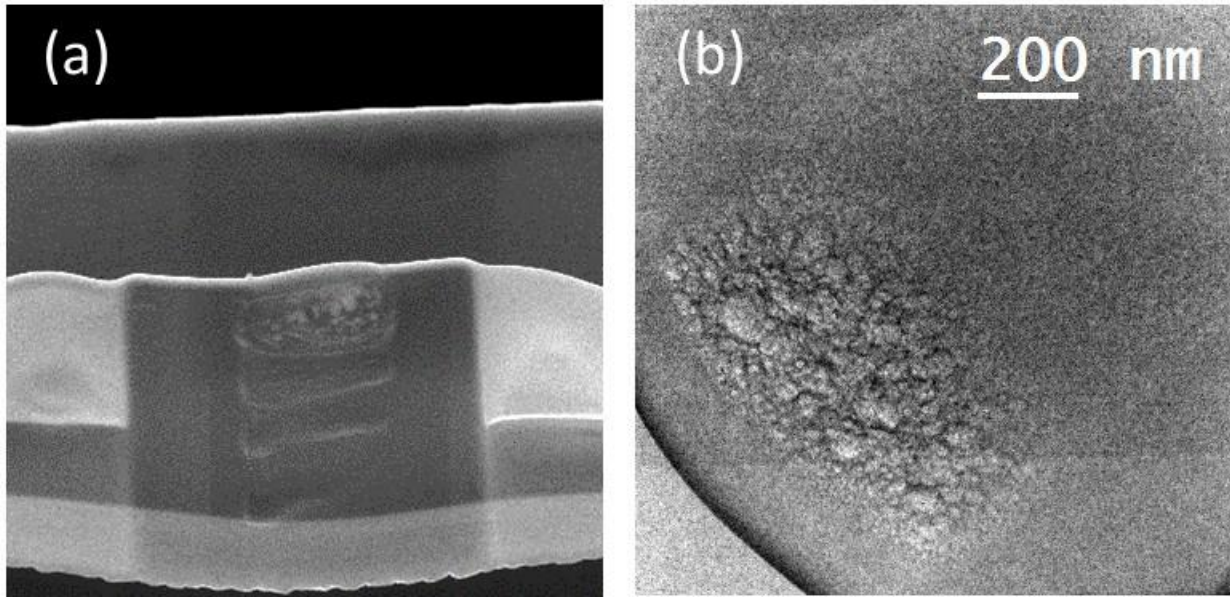
Figure S1. Example of anomalous He$^+$-induced damage in a thin diamond membrane. We fabricated the thin diamond membrane using 30 keV FGIB, and 35 keV FHIB was scanned at the edge of the membrane wall over ~ 10^{18} ion/cm^2 for the subsequent thinning of already-fabricated membrane. SEM image of 35 keV He$^+$-exposed thin membrane along the edges in (a) shows a membrane distortion with porous morphology with a bright and a dark contrast, which correspond to the existence of helium gas bubbles in the membrane, as shown in the TEM image in (b). Pressurized helium gas bubbles deformed the membrane morphology.
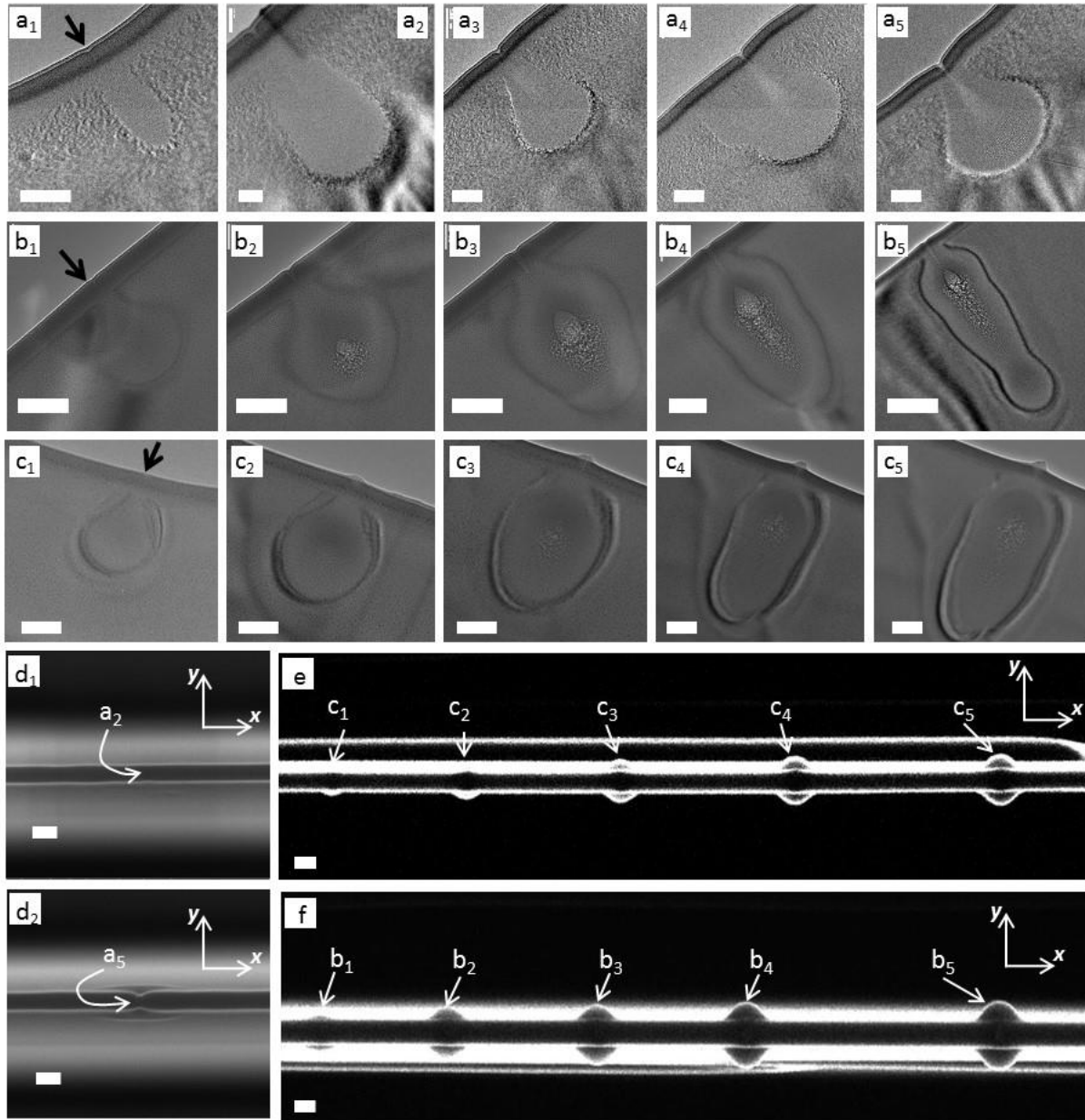
Figure S2. Cross-sectional TEM images and SEM images of three different membranes of c-Si[110], c-C[110], and c-C[100] as a function of ion dose. (a) Cross-sectional TEM images of 71-nm-thcik c-Si[110]. (b) Cross-sectional TEM images of 73-nm-thcik c-C[110]. (c) Cross-sectional TEM images of 95-nm-thcik c-C[100]. (d) SEM images of 71-nm-thcik c-Si[110]. (e) SEM images of 73-nm-thcik c-C[110]. (f) SEM images of 95-nm-thcik c-C[100]. Subscripts from 1 to 5 represent the ion dose of 8.0×10^6, 4.0×10^7, 8.0×10^7, 1.6×10^8, and 2.4×10^8 ion/point, respectively. In the manuscript, we only used c-Si[110] and c-C[110] for the comparison of dependency of materials. The direct comparison c-C[110] and c-C[100] was not adequate to investigate the

dependency of crystalline orientation due to the significant difference of the thickness, but some of measured data and observation from c-C[100] were used to investigate the dependency of crystal orientation and thickness in Figure 4.
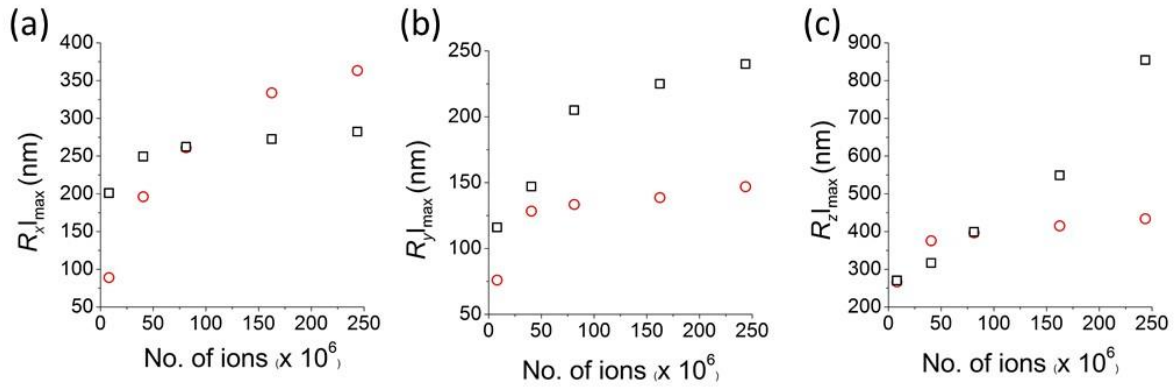
Figure S3. Measured $R_x|_{max}$, $R_y|_{max}$, and $R_z|_{max}$ for c-C (73-nm-thick) and c-Si (71-nm-thick) as a function of ion dose. $R_x|_{max}$ and $R_y|_{max}$ were measured at the first order damaged regions. The symbols □ and ○ represents c-C and c-Si, respectively.
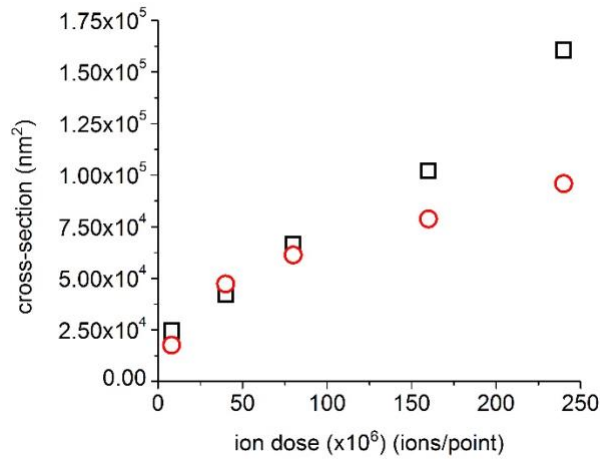
Figure S4. Measured He$^+$-induced damage region as a function of ion dose (ions/point) for c-C and c-Si membrane. The symbols □ and ○ represents c-C and c-Si, respectively.
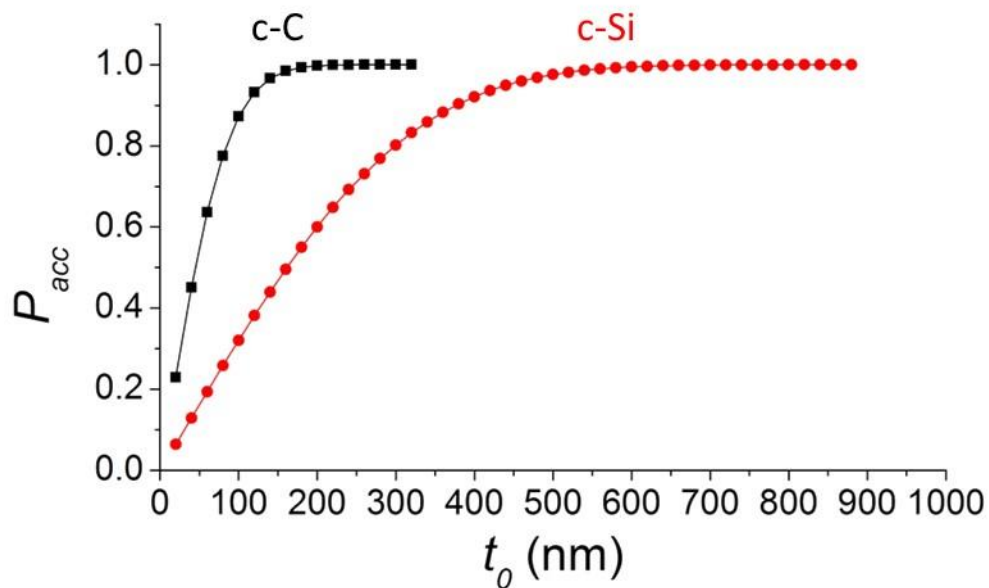
Figure S5. P_{acc} as a function of t_0 for 35 keV He⁺-exposed c-C and c-Si. This result was calculated using the SRIM.
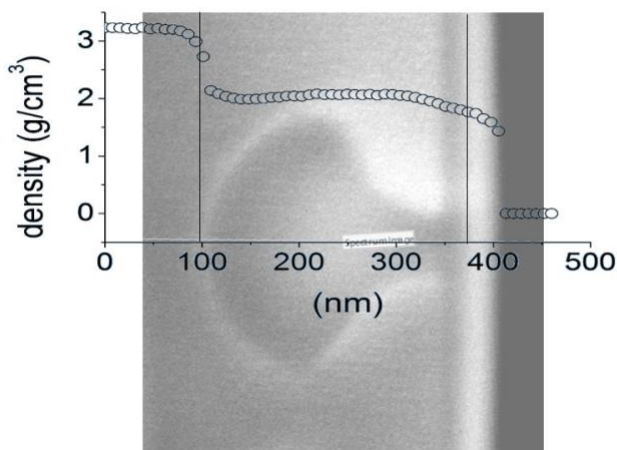
Figure S6. The estimated density of He⁺-induced damage of 73-nm-thick c-C[110] using EELS measurement. This sample corresponds to the same shown in figure 3a. The average density of He⁺-induced damage region is 2.04 g/cm³.
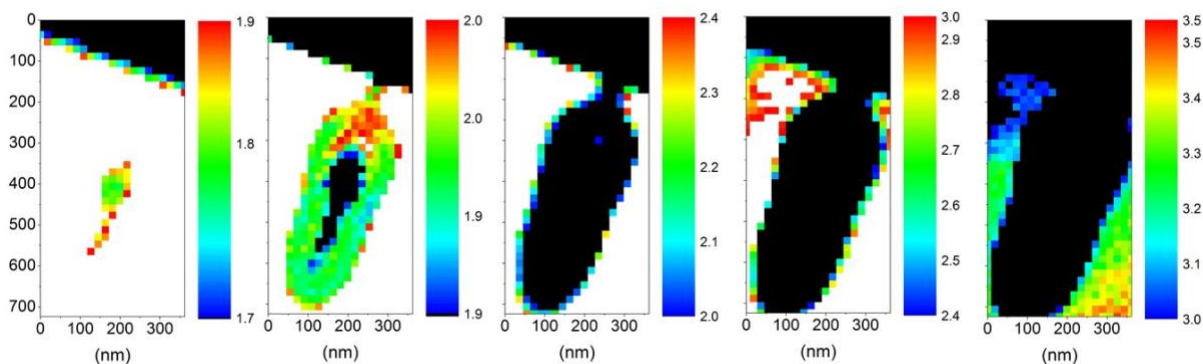
Figure S7. 2D density maps with different density ranges. The plotted density ranges are (a) $\rho = 1.72 \sim 1.89$ g/cm^3, (b) $\rho = 1.90 \sim 1.99$ g/cm^3, (c) $\rho = 2.0 \sim 2.4$ g/cm^3, (d) $\rho = 2.41 \sim 2.95$ g/cm^3, (e) $\rho = 2.96 \sim 3.47$ g/cm^3. (a-b) shows the ρ which is lower than the stable C allotropes density after ion implantation in many previous reported work.[567] (c) shows the ρ which match with the stable C allotrope density. (d) shows the ρ above the stable C allotrope density and below a higher boundary of $\rho_{\text{a-C}}$ of 2.95 g/cm^3. (e) shows the ρ of c-C.
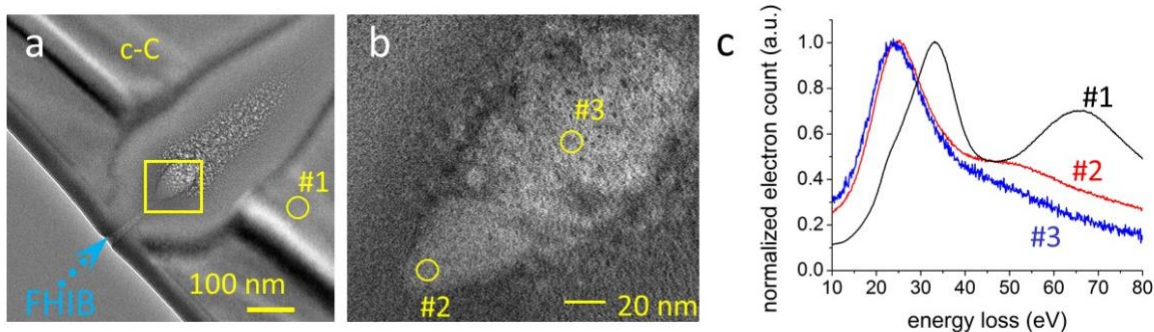
Figure S8. The estimation of density of He$^+$-damaged c-C membrane, as shown in figure 2b and figure 3e. (a) TEM image of sample used for EELS. (b) TEM image of inset in (a). Three measurement points are designated from #1 to #3. Position #1 is placed out of the damaged region, and points #2 and #3 are placed in damaged region. (c) Three measured EELS spectra as a function of energy loss. Estimated densities at each measurement point #1~#3 are 3.35 g/cm, 1.90 g/cm, and 1.78 g/cm^3, respectively. Densities in #2 and #3 are lower than the stable C allotropes density, as shown in figure S7.

9
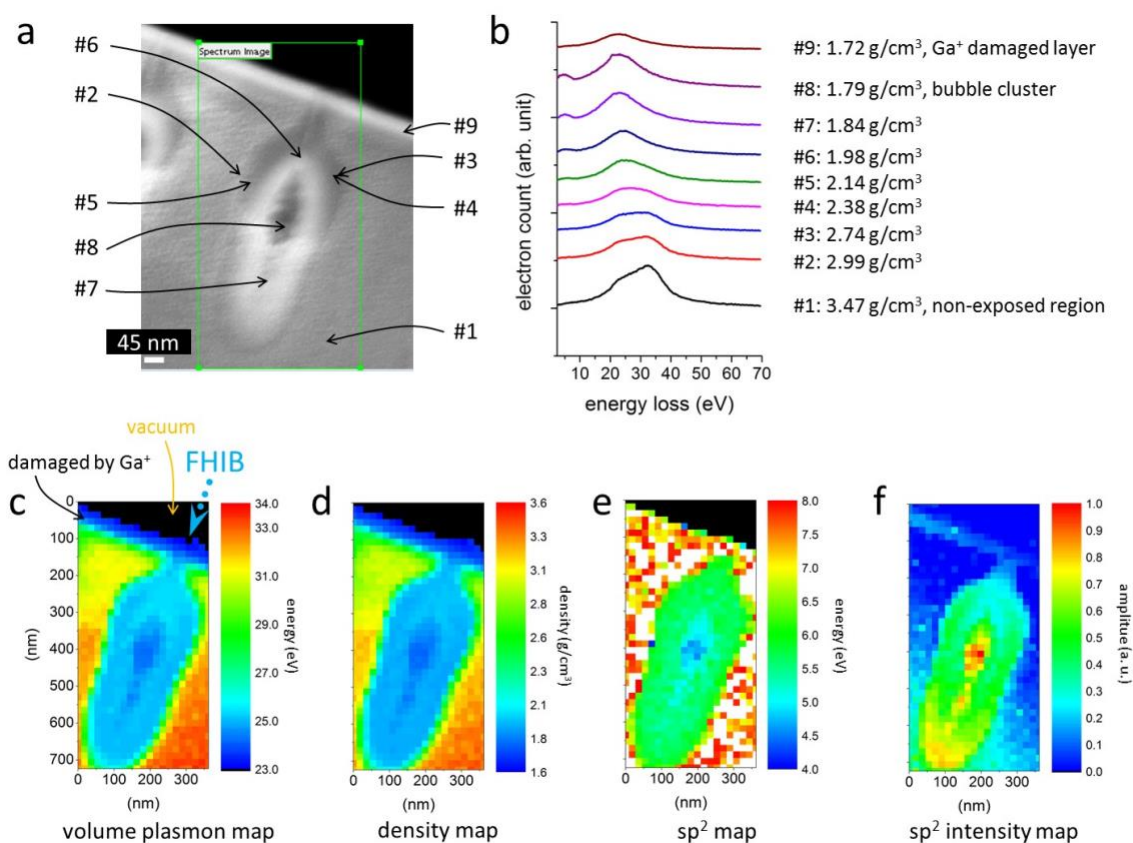
Figure S9. EELS measurement of He$^+$ scattered cross-section. (a) Scanning TEM micrograph of 35 keV He$^+$ exposed c-C with line scan (left side in figure 1b-c and figure 1e). Spectra were obtained from the green rectangular box. (b) the low energy loss spectrums from the point in (a). When the density is lower than 2.99 g/cm^3, the sp^2 peak starts to appear around 8 eV, the energy of the sp^2 peaks reduces, and the amplitude of those peaks are getting stronger. (c) 2D map of volume plasmon peak. (d) 2D map of mass density calculated from the volume plasmon energy loss peak shift. (e) 2D map of sp^2 peak energy loss shows that highly damaged region shows the lower intensity. Lower the π plasmon peak also implies that the density of π electrons is lower. (f) 2D map of the normalized sp^2 fraction shows that highly damaged region with stronger intensity. The π plasmon peak can provide alternative evidence of short-range ordering and atomic bonding. Higher fraction of π plasmon peak implies higher fraction of sp^2 clusters.
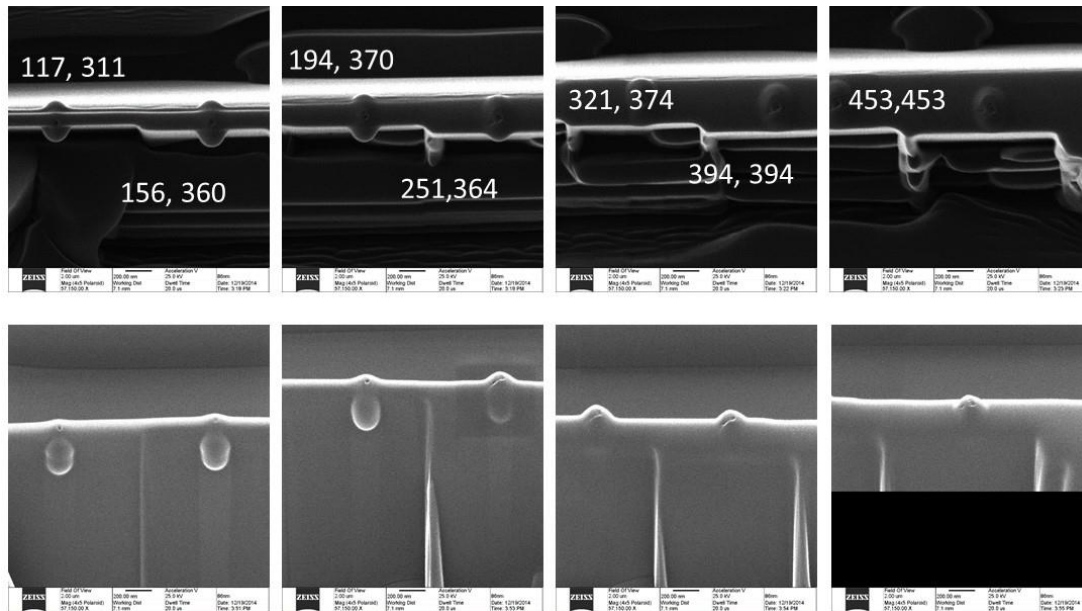
Figure S10. The t_0 and $R_y|_{max}$ (VD) measurement of 35 keV He$^+$-exposed c-C(110) sample 1.
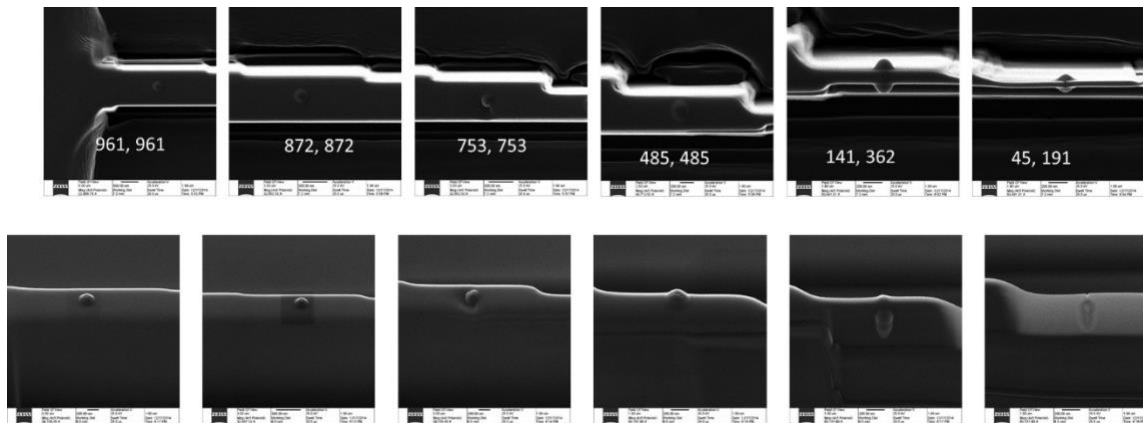
Figure S11. The t_0 and $R_y|_{max}$ (VD) measurement of 35 keV He$^+$-exposed c-C(110) sample 2.
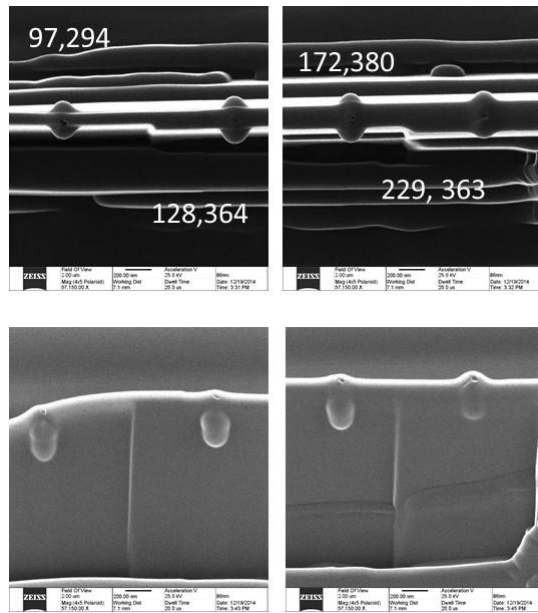
Figure S12. The t_0 and $R_y|_{\max}$ (VD) measurement of 35 keV He$^+$-exposed c-C(110) sample 3.
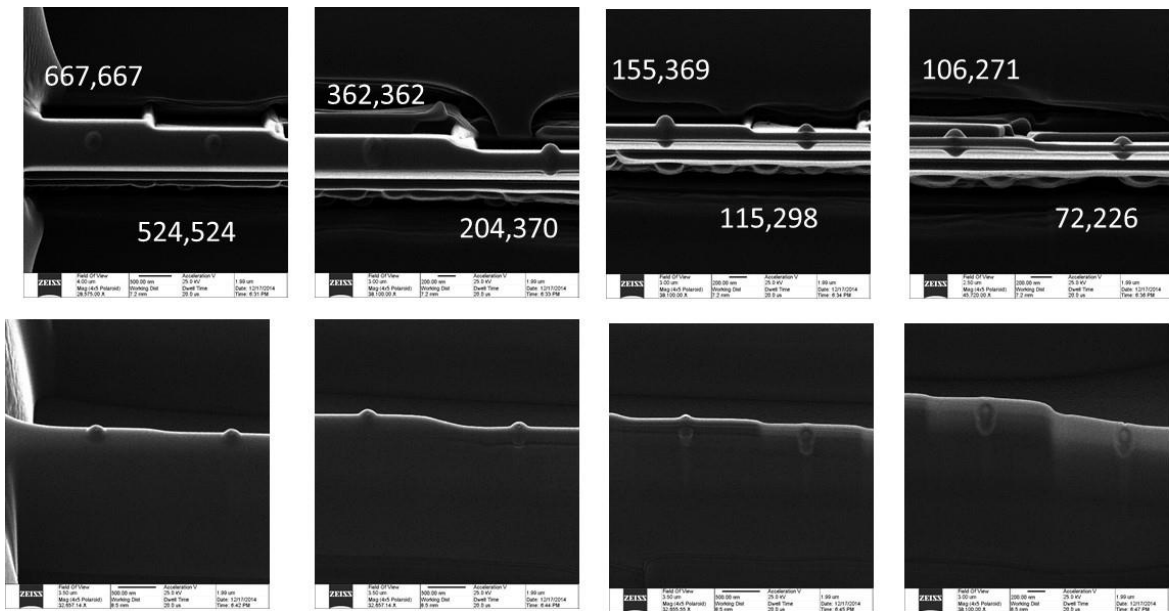
Figure S13. The t_0 and $R_y|_{\max}$ (VD) measurement of 35 keV He$^+$-exposed c-C(110) sample 4.
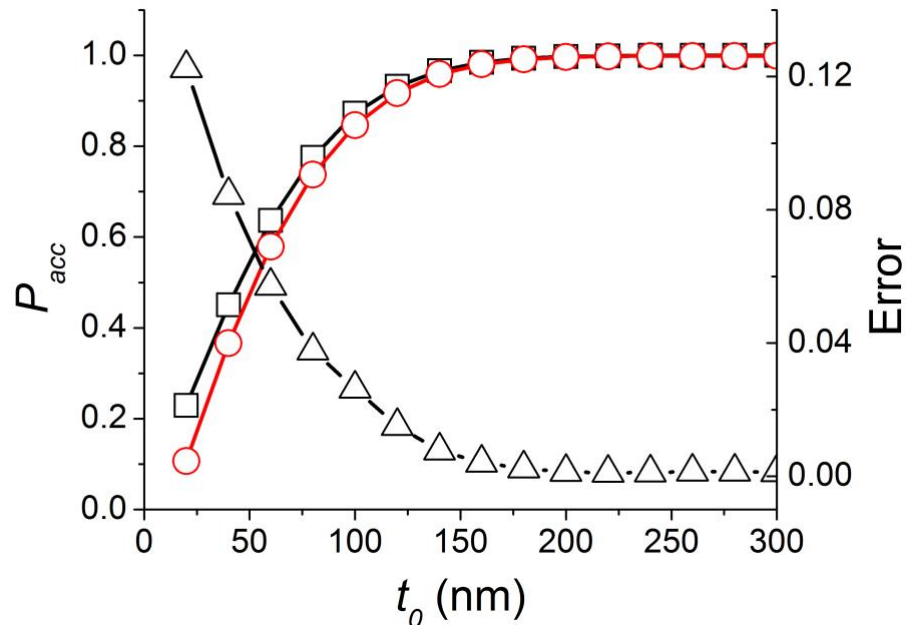
Figure S14. P_{acc}^{SRIM} and P_{acc}^{IM3D} and error P_{acc}^{SRIM}- P_{acc}^{SRIM} as a function of t_0 for He$^+$-exposed c-C. The error is due to artificial He$^+$ recoiled back to the membrane. As t_0 increases, the probability of artificial He$^+$ reduces because less He$^+$ escapes out of the membrane; thus, the error also reduces.
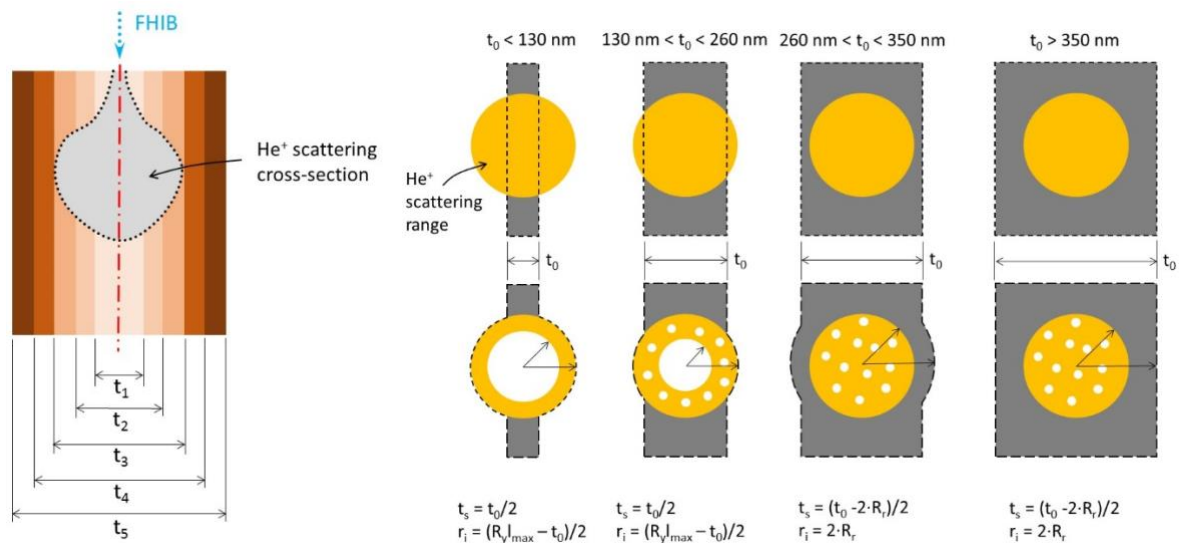
Figure S15. (a) Illustration of variation of c-C boundary conditions with the increment of t_0 without the consideration of volume deformation (VD). This is the cross-section of the *y-z* plane where a VD occurs. As the t_0 of membrane increases from t_1 to t_5, the pristine region out of the He$^+$ scattering cross-section increases. This pristine region, (which consists ofc-C), has much higher compressive and tensile strength than those of a-C. It should be noted that this illustration does not consider the volume deformation phenomena. (b) Illustration of possible variations of c-C boundary condition with the increment of t_0 with the consideration of volume deformation, and nanobubbles and bubble clusters formation. The thickness of deformed membrane (t_s) and the inner radius (r_i) change as t_0 changes.
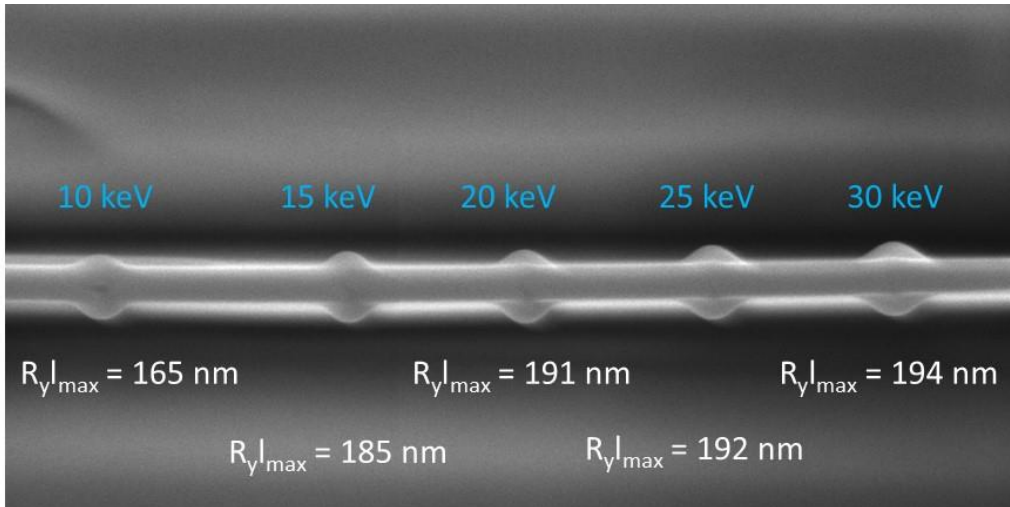
Figure S16. SEM image of He⁺-exposed 86-nm-thick c-C[100] membrane as a function of E_0 with a fixed D_0 of 8.0×10^7 ion/point.
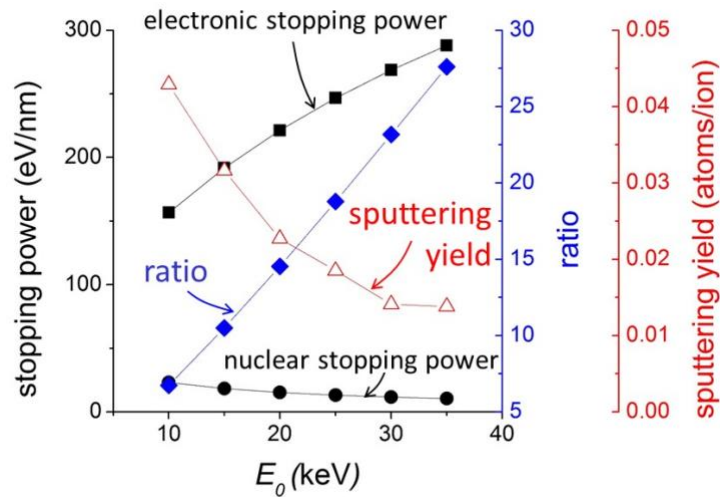
Figure S17. SRIM calculation of electronic and nuclear stopping power (eV/nm) and sputtering of c-C as a function of E_0. The ratio is calculated by electronic stopping power divided by nuclear stopping power. Thus, the ratio shows that the electronic stopping power dominates over the nuclear stopping power as E_0 increases from 10 keV to 35 keV.
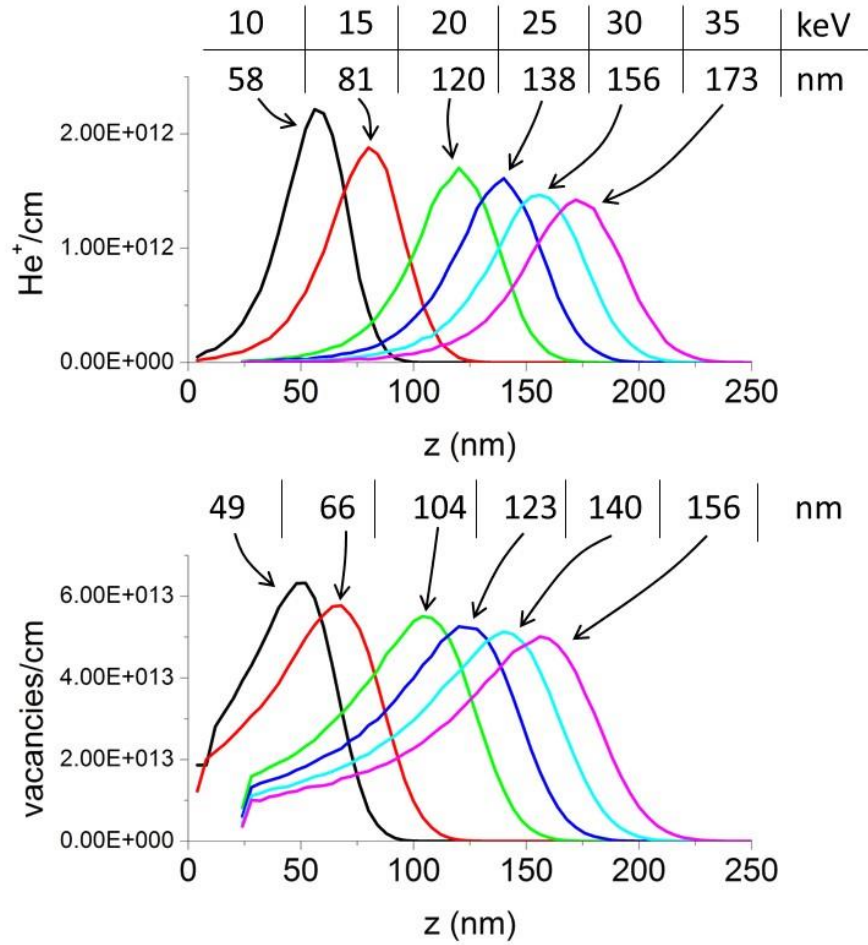
Figure S18. He$^+$ concentration and vacancy concentration as a function of E_0 along z-axis. Peak locations in the *z*-axis and the density of He$^+$ and vacancy increased and decreased, respectively as E_0 increases. This result implies that He gas bubbles are likely to be formed deeper from the surface and more He$^+$ requires to be irradiated in order to nucleate nanobubbles. He$^+$ concentration is calculated from "range.txt" having a unit of (atoms/cm^3)/(atoms/cm^2) by multiplying the 8×10^6 ions (the lowest D_0 we used). Vacancy concentration is calculated from "vacancy.txt", having a unit of vacancies/(Å·ion) by multiplying 8×10^6 ions (the lowest D_0 we used) and 10^8 (conversion from Å to cm).
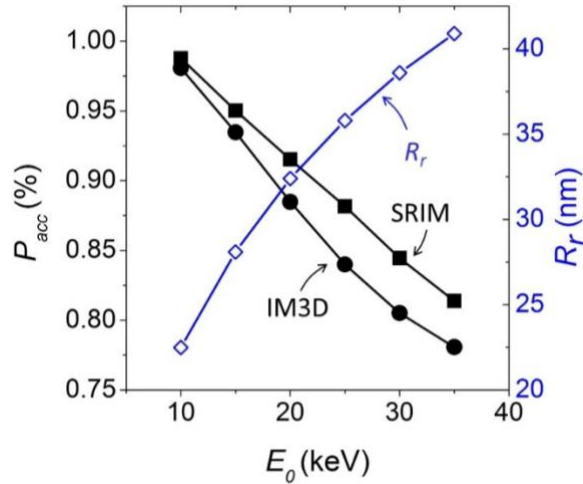
Figure S19. P_{acc} as a function of E_0 when the t_0 is 87 nm using SRIM and IM3D. The R_r, calculated using SRIM, as a function of E_0 is also plotted in order to compare with half of the membrane thickness t_0.

4. References

(1)   Robertson, J. *Mater. Sci. Eng. R Reports* **2002**, *37* (4–6), 129–281.

(2)   Ziegler, J. F.; Ziegler, M. D.; Biersack, J. P. *Nucl. Instruments Methods Phys. Res. Sect. B Beam Interact. with Mater. Atoms* **2010**, *268* (11), 1818–1823.

(3)   Li, Y. G.; Yang, Y.; Short, M. P.; Ding, Z. J.; Zeng, Z.; Li, J. *Sci. Rep.* **2015**, *5*, 18130.

(4)   Livengood, R.; Tan, S.; Greenzweig, Y.; Notte, J.; McVey, S. *J. Vac. Sci. Technol. B Microelectron. Nanom. Struct.* **2009**, *27* (6), 3244.

(5)   Fairchild, B. A.; Rubanov, S.; Lau, D. W. M.; Robinson, M.; Suarez-Martinez, I.; Marks, N.; Greentree, A. D.; McCulloch, D.; Prawer, S. *Adv. Mater.* **2012**, *24* (15), 2024–2029.

(6)   Khmelnitsky, R. A.; Dravin, V. A.; Tal, A. A.; Zavedeev, E. V.; Khomich, A. A.; Khomich, A. V.; Alekseev, A. A.; Terentiev, S. A. *J. Mater. Res.* **2015**, *30* (9), 1583–

1592.

(7)   Bosia, F.; Argiolas, N.; Bazzan, M.; Fairchild, B. A.; Greentree, A. D.; Lau, D. W. M.;

         Olivero, P.; Picollo, F.; Rubanov, S.; Prawer, S. *J. Phys. Condens. Matter* **2013**, *25* (38),

         385403.